The Astrophysical Journal, 960:54 (21pp), 2024 January 1 https://doi.org/10.3847/1538-4357/acfe6f

When and How Ram Pressure Stripping in Low-mass Satellite Galaxies Enhances Star Formation

Jingyao Zhu[1], Stephanie Tonnesen[2], and Greg L. Bryan[1,2]
[1] Department of Astronomy, Columbia University, New York, NY 10027, USA; jingyao.zhu@columbia.edu
[2] Center for Computational Astrophysics, Flatiron Institute, New York, NY 10010, USA
Received 2023 June 6; revised 2023 September 11; accepted 2023 September 27; published 2023 December 21

Abstract

We investigate how a satellite's star formation rate (SFR) and surviving gas respond to ram pressure stripping (RPS) in various environments. Using a suite of high-resolution *wind tunnel* simulations with radiative cooling, star formation, and supernovae feedback, we model the first infall orbit of a low-mass disk galaxy ($M_* = 10^{9.7}\,M_\odot$) in different host halos, ranging from Milky Way–like to cluster hosts. When the ram pressure is moderate, we find that the stripping satellite shows an enhanced SFR relative to the isolated control case, despite gas loss due to stripping. The SFR enhancement is caused, not directly by compression, but by ram-pressure-driven mass flows, which can increase the dense gas fraction in the central disk regions. The spatially resolved star formation main sequence and Kennicutt–Schmidt relations in our simulations are consistent with recent findings of the VERTICO and GASP surveys. Our results predict the environmental signals of RPS in future multiwavelength, high-angular resolution observations: the star formation and gas surface densities will be centralized, and symmetrically enhanced within the stripping radius.

Unified Astronomy Thesaurus concepts: Interstellar medium (847); Galaxy interactions (600); Star formation (1569); Hydrodynamical simulations (767)

1. Introduction

A galaxy can either be star forming or quenched, depending on internal and environmental processes (Kauffmann et al. 2004; Baldry et al. 2006; Peng et al. 2010). For the central galaxies within halos, internal processes such as supernova and active galactic nucleus feedback are the main star formation regulators (Croton et al. 2006; Dalla Vecchia & Schaye 2008). This explains the *main sequence* of star formation over cosmic time: a tight correlation between the star formation rate (SFR) and stellar mass (M_*) of galaxies (Speagle et al. 2014). For satellite galaxies, environmental factors from the interactions with a central halo become significant: satellites show a strong observational bias to be *red*, or star formation quenched, compared with their central counterparts at the same stellar masses (Peng et al. 2012; Wetzel et al. 2012; Phillips et al. 2014). The environmental quenching of satellite galaxies is also ubiquitous in cosmological simulations (Tremmel et al. 2019; Wright et al. 2019; Appleby et al. 2020; Donnari et al. 2021a, 2021b).

Despite the consensus of environmental quenching in observations and simulations, uncertainties remain in the mass dependence and the scatter of the quenching effectiveness (Donnari et al. 2021b). The uncertainties likely arise from the complex physical processes during the satellite–environment interactions (see the recent review by Cortese et al. 2021), of which the dominant is RPS (Gunn & Gott 1972), the direct removal of the satellite's interstellar medium (ISM) by a host halo medium. RPS galaxies, identified by unidirectional gas tails and little stellar disk deformation, have been observed in several clusters (van Gorkom 2004; Boselli et al. 2006; Sun et al. 2007; Poggianti et al. 2016; Deb et al. 2022) as well as in both idealized (e.g., Abadi et al. 1999; Quilis et al. 2000; Schulz & Struck 2001; Roediger & Brüggen 2006; Jáchym et al. 2007; McCarthy et al. 2008) and cosmological simulations (Bahé et al. 2012; Yun et al. 2019; Rohr et al. 2023). Although the hallmark of RPS is gas removal, and therefore, the eventual quenching of star formation (Boselli et al. 2006; Crowl & Kenney 2008), recent detailed observations have shown that the early stages of RPS may have complex effects on both the ISM phase distribution and SFRs. Under RPS, the satellite's star formation can be triggered (Ebeling et al. 2014; Jáchym et al. 2019; Poggianti et al. 2019), the SFR globally (Vulcani et al. 2018; Roberts et al. 2021; Kolcu et al. 2022; Molnár et al. 2022) or locally (Vulcani et al. 2020) enhanced, and the molecular-to-atomic gas ratio boosted (Moretti et al. 2020).

The interplay between RPS and star formation is key to understanding environmental quenching, and has been explored in various controlled hydrodynamical simulations. Multiple simulations analyzed the question of RPS-triggered or enhanced star formation (Schulz & Struck 2001; Kapferer et al. 2009; Tonnesen & Bryan 2012; Bekki 2014; Roediger et al. 2014; Steinhauser et al. 2016; Ruggiero & Lima Neto 2017; Lee et al. 2020), but the physical reasons behind the enhancement are unclear. Ram-pressure-driven shock passages can trigger local boosts to the SFR, but have little global effects (Roediger et al. 2014); pressure enhancement in the wind-leading halves of the galaxies undergoing stripping suggests that compression likely enhances the star formation efficiency (Troncoso-Iribarren et al. 2020; Roberts et al. 2022); ram-pressure-induced radial gas inflows can modify the star formation morphology, shifting it to the central regions with higher SFR (Schulz & Struck 2001; Tonnesen & Bryan 2012; Lee et al. 2020). There is a need to examine the physical causes of RPS-enhanced star formation in simulations, and to directly compare with recent observations.

In this work, we study the complicated effects of RPS on the ISM distribution and SFRs. (i) We simulate a low-mass spiral galaxy (lowest resolved in Donnari et al. 2021b, with tension in the quenched fractions) undergoing RPS in different environments, from a Milky Way–like to a cluster halo, and examine the galaxy's gas and SFR response; (ii) For each host halo, we model a realistic infall orbit with time-varying ram pressure profiles; (iii) We analyze the local SFR–mass relations at comparable spatial resolutions with recent high-angular resolution observations (Vulcani et al. 2020; Jiménez-Donaire et al. 2023); and finally (iv) We compare and identify key physical causes of RPS-enhanced star formation.

The structure of this paper is as follows. In Section 2, we introduce the methodology, with Section 2.1 on the satellite galaxy model, Section 2.2 on the infall orbits, and Section 2.3 the simulations' initial conditions. We present the global simulation results in Section 3: the time evolution of star formation and the surviving gas (Section 3.1), and the gas morphology and kinematics (Section 3.2). Then, Section 4 compares the spatially resolved SFR–mass relations ($\Sigma_{\rm SFR}$–$\Sigma_{\rm gas}$ and $\Sigma_{\rm SFR}$–Σ_{*}) between the stripping and isolated galaxy sets. We discuss our results in Section 5: the impact of RPS on star formation (Section 5.1), predictions for observations (Section 5.2), and limitations of our methodology (Section 5.3). Section 6 summarizes the key findings.

2. Methodology

We run a suite of three-dimensional *wind tunnel* simulations using the adaptive mesh refinement (AMR) code Enzo (Bryan et al. 2014). The simulation volume is a 162^3 kpc cube with a 128^3 root grid resolution. We allow up to five levels of refinement, giving the highest spatial resolution of 39 pc (marginally resolving giant molecular clouds). To model the radiative cooling of the multiphase gas, we use the Grackle chemistry and cooling library[3] (Smith et al. 2017), which calculates photoheating and photoionization from the UV background of Haardt & Madau (2012). We use the star formation recipe of Goldbaum et al. (2015) with the following parameters: once a gas cell reaches the Jeans criterion with a number density threshold of $n_{\rm min} = 10\,{\rm cm}^{-3}$, it forms star particles (including regular stars and Type II supernovae) with a 5% efficiency. The star particles, now followed in our simulations as active particles, subsequently deposit energy into the gas in the forms of stellar and supernovae feedback, under the Goldbaum et al. (2016) feedback model, which includes the terminal momentum input from the number of supernovae expected to go off during a given time step, adding any additional energy in the form of thermal energy.

We use yt, a multi-code toolkit for analyzing and visualizing astrophysical simulation data (Turk et al. 2011), to create slices and projections, and to select the disk gas and the active star particles for subsequent analyses.

2.1. The Galaxy

Our galaxy is placed at the center of the 162 kpc cubical simulation volume at (81, 81, 81) kpc. We choose a galaxy of low-stellar mass $M_{*} = 10^{9.7}\,M_{\odot}$, motivated by the lowest satellite M_{*} examined in Donnari et al. (2021b) using the IllustrisTNG cosmological simulations (Weinberger et al. 2017; Pillepich et al. 2018). Table 1 summarizes the global parameters of the satellite galaxy.

[3] https://grackle.readthedocs.io/

Table 1
Global Parameters of the Low-mass Galaxy

Stellar Disk			Dark Matter		Gas Disk		
M_{*} ($M_{\odot}$)	a_{*} (kpc)	b_{*} (kpc)	ρ_{d0} (g cm^{-3})	r_0 (kpc)	$M_{\rm gas}$ ($M_{\odot}$)	$a_{\rm gas}$ (kpc)	$b_{\rm gas}$ (kpc)
$10^{9.7}$	2.5	0.5	5.93e-25	11.87	$10^{9.7}$	3.75	0.75

Among the three components in Table 1, our simulations model the stellar disk and dark matter as static gravitational potential fields. The static stellar disk potential is under the Plummer–Kuzmin model (Miyamoto & Nagai 1975) with the scale length (a_{*}) and height (b_{*}) of 2.5 and 0.5 kpc, respectively (from the baryonic mass–stellar disk size scaling relation; Wu 2018). We model the cold dark matter potential under the spherical Burkert model (Burkert 1995; Mori & Burkert 2000), which is selected to better match the observational rotation curves of low-mass galaxies (Salucci & Burkert 2000; de Blok et al. 2008). Given the stellar mass (Table 1), we obtain the circular velocity $V_{\rm circ} \approx 120$ km s^{-1} from the observational baryonic Tully–Fisher relation (Lelli et al. 2019; McGaugh et al. 2021), which gives the dark matter central density ρ_{d0} and scale radius r_0 (Table 1).

The gas disk in Table 1 is followed in our simulations with AMR. We adopt the gas mass from observed gas-(H I and H_2 combined) to-stellar mass ratio $M_{\rm gas}/M_{*} \approx 1$ (Calette et al. 2018), and the disk size from the size ratio $R_{\rm gas}/R_{\rm optical} \approx 1.25$ (Swaters et al. 2002). This ensures that the resulting galaxy model is consistent with the $z \approx 0$ observed scaling relations. The gas density is distributed under a softened exponential disk model (see Tonnesen & Bryan 2009, 2010, Equation (1)), and the temperature and pressure are calculated to maintain hydrostatic equilibrium in the disk with the surrounding ICM. The rotational velocity is then calculated to balance the gravitational force and the combination of the centrifugal force and the pressure gradient.

2.2. The Orbits

We model the time-varying infalling orbits—satellites traveling from the host's virial radius R_{200} to the pericenter location $R_{\rm peri}$—of three host halos: a *Milky Way–like* host halo of $M_{200} = 10^{12}\,M_{\odot}$, a *group* halo of $M_{200} = 10^{13}\,M_{\odot}$, and a *cluster* halo of $M_{200} = 10^{14}\,M_{\odot}$. The host mass selection is motivated by the mass-dependent quenched fraction disagreements in Donnari et al. (2021b): a satellite of $M_{*} = 10^{9.7}\,M_{\odot}$ tends to be under-quenched in the TNG300 simulations compared with the Sloan Digital Sky Survey (SDSS) observations for the low-mass hosts $M_{200,\rm host} < 10^{13.5}\,M_{\odot}$, but over-quenched in simulations for the higher mass hosts (see Donnari et al. 2021b, Figure 9). Our host mass sampling ($M_{200,\rm host} \in [10^{12},\ 10^{14}]\,M_{\odot}$) is to span the mass range over which the Donnari et al. (2021b) turnover in quenching effectiveness happens for the satellite of $M_{*} = 10^{9.7}\,M_{\odot}$.

In this subsection, we describe our two-step orbit modeling process: (1) satellite orbit kinematics (Table 2), which gives the position and velocity of the satellite galaxy as a function of infalling time; and (2) host halo radial profiles (Table 3), which

Table 2
Parameters of the Satellite Galaxy Infalling Orbits

M_{200} ($M_\odot$)	Case	c	R_{200} (kpc)	$R_{\rm peri}$ (kpc)	V_{200} (km s^{-1})	($\lvert V_{\phi,0}\rvert$, $\lvert V_{r,0}\rvert$) V_{200}	$V_{\rm peri}$ (km s^{-1})	e	$\tau_{\rm infall}$ (Myr)
	(1)	(2)	(3)	(4)	(5)	(6)	(7)	(8)	(9)
10^{12}	Milky Way	8.81	211	75	143	(0.655, 0.832)	265	0.674	1127
10^{13}	Group	7.08	455	149	308	(0.603, 0.786)	565	0.666	1165
10^{14}	Cluster	5.62	949	278	663	(0.53, 0.782)	1236	0.692	1164

Note. Column (1) The case names represent the physical context of the central halos. Column (2) The present-day (redshift-zero) concentration values c from Ludlow et al. (2014). Columns (3), (4), (7) The virial radii (R_{200}), the pericentric radii ($R_{\rm peri}$), and velocities ($V_{\rm peri}$) from the Gala-generated orbits, see Section 2.2. Column (5) The virial velocities defined as $V_{200} \equiv \sqrt{G \cdot M_{200}/R_{200}}$, following Wetzel (2011). Column (6) The tangential ($\lvert V_{\phi,0}\rvert$) and radial ($\lvert V_{r,0}\rvert$) velocity magnitudes at R_{200} in units of the virial velocity (V_{200}; see Column (5)) from Wetzel (2011), used as velocity initial conditions for the orbit integration. Column (8) The resulting orbital eccentricities. Column (9) The infalling time from R_{200} to $R_{\rm peri}$.

Table 3
Parameters of the Hosts' Gaseous Halo Profiles

Case	$n_0 r_c^{3\beta}$ (10^{-2} cm^{-3} kpc$^{3\beta}$)	C (kpc)	β	T (K)	References
(1)	(2)	(3)	(4)	(5)	(6)
Milky Way	1.35	2.73	0.5	2.51E6	MB15
Case	n_0 (cm^{-3})	r_c (kpc)	β	T (K)	References
Group	0.0121	25	0.655	5.53e6	KS01
Cluster	0.0071	76	0.675	2.02e7	KS01

Note. Column (1) Case names as in Table 2. We list the Milky Way case separately from the group and cluster cases because of the different methods; see Section 2.2. Column (2) Best-fit parameter $n_0 r_c^{3\beta}$ for the modified β profile of Miller & Bregman (2015), which fits n_0 and r_c of a β profile together (Equations (1) and (2)); or n_0 for the group and cluster cases. Column (3) The constant factor C in Equation (2) to match with the LMC-constrained pericentric conditions of the Milky Way halo (Salem et al. 2015); or r_c for the group and cluster cases. Column (6) References for our adopted β-profile (or modified in the Milky Way case) parameters, β, r_c, and the isothermal gas halo temperatures T. MB15: Miller & Bregman (2015); KS01: Komatsu & Seljak (2001).

gives the density and temperature of the host's gaseous halo medium as a function of radius.

We use the Galactic Dynamics package Gala (Price-Whelan 2017; Price-Whelan et al. 2020) to perform time integration of the satellite orbits. First, we use Gala to construct the three host halos' gravitational potential profiles, adopting a Navarro–Frenk–White (NFW) halo structure (Navarro et al. 1996), and redshift-zero concentration values (c in Table 2; Ludlow et al. 2014). For simplicity, we assume that the satellite travels as a point mass when orbiting the host halos. The orbital integration begins at the host's virial radius R_{200} (from the Gala-generated NFW profiles), and takes the best-fit values of Wetzel (2011) as velocity initial conditions, see ($\lvert V_{\phi,0}\rvert$, $\lvert V_{r,0}\rvert$)/V_{200} in Table 2. With the position and velocity initial inputs, we then use the Gala orbital integrator to integrate for a sufficient time (e.g., 100 Gyr) to ensure we capture many stable orbits, and focus on the branch from R_{200} to pericenter $R_{\rm peri}$. The resulting orbits contain the satellite's position and velocity as a function of infalling time, as summarized in Table 2.

We model the extended, diffuse gaseous halos of the hosts as an isothermal sphere with a β-profile in density (Cavaliere & Fusco-Femiano 1976; Arnaud 2009). The spherical-β model is a relatively simple three-parameter model capable of reproducing the X-ray surface brightness observations for a range of galaxies (Makino et al. 1998; O'Sullivan et al. 2003; Anderson & Bregman 2011; Dai et al. 2012). It gives the gaseous halo density at a distance r from the center as

$$n(r) = n_0 \cdot \left[1 + \left(\frac{r}{r_c}\right)^2\right]^{-3\beta/2}, \quad (1)$$

where n_0 is the core density, r_c is the core radius, and β is the density slope at large radii. Among our three host cases, we apply the generic β modeling for the group and cluster cases, but it breaks down at the low mass of $10^{12}\,M_\odot$, where we instead use observational data of the Milky Way (Miller & Bregman 2013, 2015; Salem et al. 2015; Voit 2019). The parameters of the halo models are summarized in Table 3 below.

For the Milky Way host case, we refer to the Miller & Bregman (2015) parameterization of a modified β profile,

$$n(r) \approx \frac{n_0 r_c^{3\beta}}{r^{3\beta}}, \quad (2)$$

where n_0, r_c, and β are defined as in Equation (1) above (see Miller & Bregman 2015, Equation (2)). However, this profile becomes less constrained at the large radii of our satellite's orbit (Table 2), and tends to underestimate densities compared with other studies (see Voit 2019, Figure 3). To address this density underestimation at large radii, we boost the best-fit Miller & Bregman (2015) model by a constant factor $C \approx 2.73$, obtained by matching the LMC-constrained pericentric (at 48.2 kpc) density from Salem et al. (2015).

For the galaxy group and cluster cases, we obtain the three parameters in the β model (Equation (1)) as follows: we adopt r_c and β from the gas halo profiles of Komatsu & Seljak (2001), and solve for n_0 as an integration constant by assuming the gas-to-total mass fraction at R_{500} is ≈10% (Lovisari et al. 2015; $f_{\rm gas,500} = M_{\rm gas,500}/M_{\rm tot,500} \approx 10\%$). The gas mass within R_{500} under a β profile in density (Equation (1)) can be written as,

$$M_{\rm gas,500} = 4\pi\rho_{\rm gas,0}\int_0^{R_{500}}\left[1 + \left(\frac{r}{r_c}\right)^2\right]^{-3\beta/2} r^2 dr \approx 10\% \cdot M_{\rm tot,500}, \quad (3)$$

where we supply r_c, β from Komatsu & Seljak (2001), $M_{\rm tot,500}$ and R_{500} from the Gala-generated host NFW halos, and the $f_{\rm gas,500} \approx 10\%$ relation from Lovisari et al. (2015). Solving

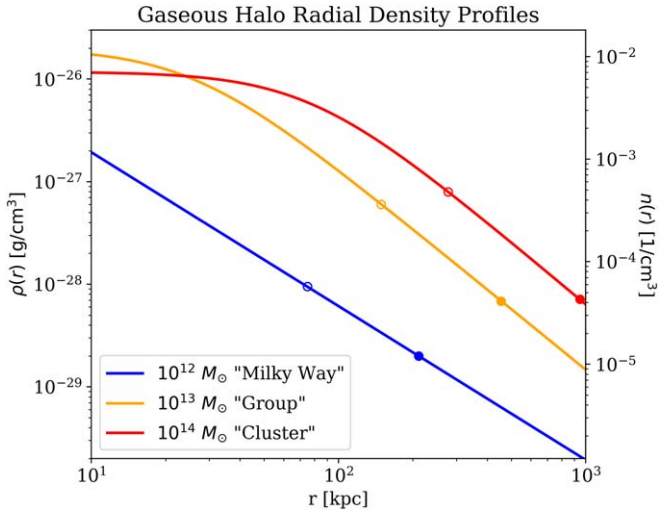

Figure 1. The radial density profiles of the three gaseous host halos in this study (Table 3). Solid and empty circles show the virial radii (R_{200}) and pericenter radii ($R_{\rm peri}$), respectively, which mark the initial and final locations of the satellite infall orbits (see Table 2). The y-axis on each side shows the same information in mass density (left: ρ) and number density (right: n).

Equation (3) for the integration constant $\rho_{\rm gas,0}$ gives the central mass density and hence the number density n_0.

Figure 1 shows the density profiles of the three gaseous halo cases shown in Table 3, where we annotate the infall orbits' initial (virial radius) and final (pericenter) locations from Table 2. At a given time t of an infall orbit, the orbital density is given by the density profiles $\rho(r)$ in Figure 1, taking the radius $r(t)$ from the Gala-generated orbits. The resulting orbital density ranges (densities between the solid and empty circles in Figure 1) for the group and the cluster cases are relatively similar, but the cluster case has a higher pericentric velocity (Table 2), which leads to about five times the ram pressure of the group case at the pericenter, see Section 2.3 below for details.

2.3. The Simulations

Our suite of four simulations includes three *wind tunnel* runs and one *isolated galaxy* run. In each of the wind tunnel runs, we introduce a 45° inclined boundary inflow (velocity normal vector $\hat{v}_{{\rm wind}(x,y,z)} = (0, \frac{\sqrt{2}}{2}, \frac{\sqrt{2}}{2})$) from the $y = 0, z = 0$ corner of the simulation box. Instead of a purely face-on or edge-on wind, we choose the 45° inclination angle to investigate the ram pressure effects both perpendicular and parallel to the disk. The inflow is modeling the ram pressure *wind*, which carries the time-varying orbital conditions (gas density, temperature, and velocities) set in Section 2.2. The metallicities of the inflow gas (the wind) and the initial galaxy gas disk (see Section 2.1) are set as $Z_{\rm wind} = 0.1\,Z_\odot$ and $Z_{\rm galaxy} = 0.3Z_\odot$, respectively, which are subsequently used as tracers for galactic versus wind material. The isolated galaxy run is a control case without inflow, but otherwise has the same setup of galaxy structure, radiative cooling, star formation, and feedback as in the wind runs.

We summarize key aspects of the simulations in Table 4 and Figure 2. The time-dependent ram pressure is defined as $P_{\rm ram}(t) = \rho_{\rm host}(t) \cdot v_{\rm sat}(t)^2$, where the host halo medium density (Figure 1) $\rho_{\rm host}(t)$ is evaluated at the satellite location $r_{\rm sat}(t)$; and the satellite location and velocity, $r_{\rm sat}(t)$ and $v_{\rm sat}(t)$,

Table 4
Overview of the Simulation Suite

Simulation	$P_{{\rm ram},i}$ (g/(cm s^2))	$P_{{\rm ram},f}$ (g/(cm s^2))	t_i (Myr)
(1)	(2)	(3)	(4)
12W	4.6e-15	6.7e-14	0
13W	6.4e-14	1.9e-12	1060
14W	2.6e-13	1.2e-11	1600
iso	…	…	0

Note. Column (1) Abbreviated simulation names used throughout this paper. 12W: Milky Way halo ($10^{12}\,M_\odot$) wind; 13W: group halo ($10^{13}\,M_\odot$) wind; and 14W: cluster halo ($10^{14}\,M_\odot$) wind; iso: isolated galaxy (no wind). Columns (2) and (3) The initial and final ram pressure values of the wind orbits (Section 2.2), also see Figure 2. Column (4) The initial time of each simulation. 12W and iso both begin at $t = 0$, but the 13W and 14W runs are each continued from a lower halo mass case's evolved snapshot with matching ram pressures. For example, the 13W run is a continuation from the $t = 1060$ Myr snapshot of 12W, where the initial ram pressure $P_{{\rm ram},i({\rm 13W})}$ matches the 12W run's $P_{{\rm ram},t=1060({\rm 12W})}$, see Figure 2.

are from the Gala-generated orbits (Section 2.2 and Table 2). For the three wind runs (hereafter 12W, 13W, and 14W), we list the initial and final ram pressure values from the orbits described in Section 2.2, and show their time evolution in Figure 2. We initialize the 13W run from a snapshot in the 12W run where the ram pressure matches the 13W initial conditions, and similarly start the 14W run from a 13W snapshot; see the relevant time frames in Figure 2. This results in the initial galaxy disk in the 13W and 14W runs being *preprocessed*: it has been orbiting in smaller host halos prior to its accretion onto the more massive group or cluster host, a highly probable process for low-mass galaxies that has abundant observational and theoretical evidence (Zabludoff et al. 1996; Wetzel et al. 2013; Haines et al. 2015; Jung et al. 2018; Bahé et al. 2019; Donnari et al. 2021a). For the masses modeled in this paper, TNG simulations find ≈50% of satellites below $M_* = 10^{10}\,M_\odot$ have been preprocessed in hosts of $M_{200} = 10^{12}\,M_\odot$ or above, if they reside in a cluster of $M_{200} = 10^{14}\,M_\odot$ at $z = 0$ (Donnari et al. 2021a).

Initializing the simulations from a previous snapshot effectively avoids the numerical artifacts in the initial few hundred megayears, like an unstable outburst of star formation (Tasker & Bryan 2006) and significant transient ringing (Goldbaum et al. 2015) in the gas disk. Previous works such as that of Tonnesen & Bryan (2012) addressed these artifacts by delaying the wind and allowing for a thermal relaxation phase of at least 200 Myr to stabilize the disk. For our 12W run (the only wind simulation that begins at $t = 0$); however, the wind delay is unnecessary. Because of the Milky Way wind's initial slow speed ($|v_{\rm wind}| \approx 151$ km s^{-1}; Table 2), it takes the first shock wave (of Mach number 2) generated by the initial inflow more than 300 Myr to reach the galaxy disk, and longer for the stable inflow, see Figure 2. The location of the sampling box for ram pressure values (right panel of Figure 2) is chosen to be relatively close to the galactic disk, while avoiding the bow shock in front of the galaxy after the thermal relaxation phase.

The three wind runs cover over three orders of magnitude in ram pressure (solid lines in Figure 2), which generally follow the input orbit conditions (dashed lines). We attach a constant ram pressure value at the end of each wind run to ensure the pericentric inflow from the corner of the simulation box reaches

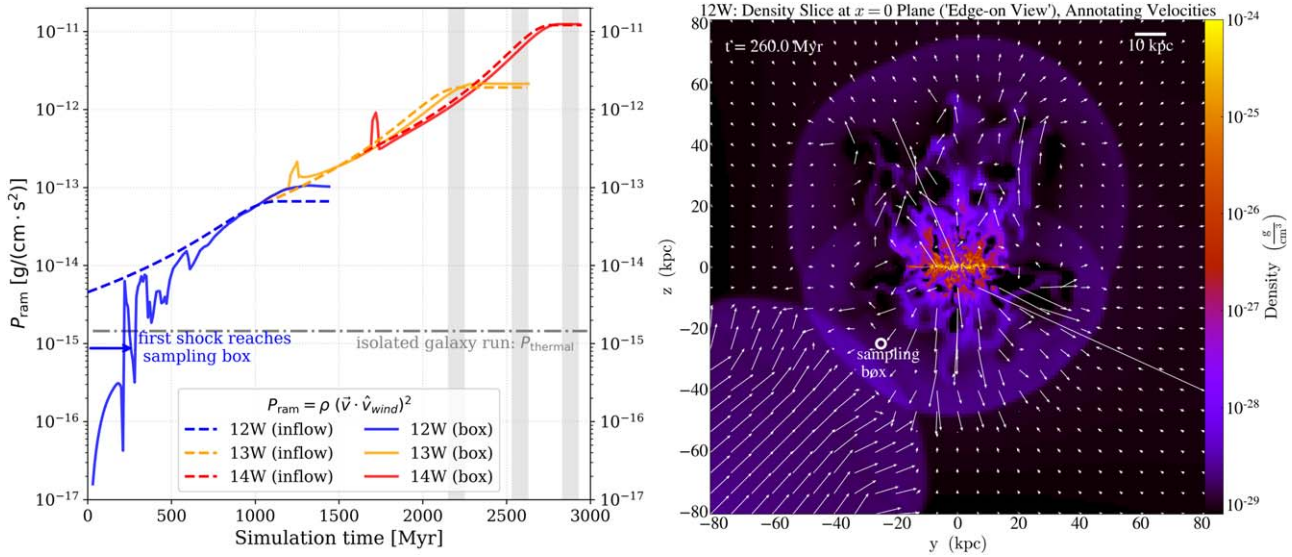

Figure 2. Left: ram pressure time evolution for the three wind simulations. Dashed lines show the input from the orbits (Sections 2.2 and 2.3), solid lines indicate the simulation values ($\rho \cdot v_{gas}^2$ in the wind direction $\hat{v}_{wind}$) read in from a sampling box (see the right panel). The dashed–dotted gray line shows the ambient gas thermal pressure in the isolated run for reference. The three shaded vertical bars denote important time frames we will later refer to in Figure 3 and Section 3. Right: a density slice of the 12W Milky Way case, annotating in-plane gas velocities. The inflow wind from the lower left corner travels at low velocities (Table 2), taking 200–300 Myr to reach the sampling box (white circle; at (0, −25, −25) kpc), and another 100–200 Myr to reach the disk (domain center). The inflow is about to reach the sampling box at this snapshot.

the galactic disk, and the attached time periods are relatively short (<300 Myr). We annotate the input intracluster medium (ICM) thermal pressure of the isolated case as the dashed–dotted line in Figure 2, which is lower than the weakest ram pressure input of the wind runs ($t = 0$ of 12W). The sampled ram pressure of 12W (blue solid line) is low during 0–300 Myr because it shows the initial collapse of the gas before the wind reaches the sampling box; then during ∼300–700 Myr, its stochasticity reflects an interplay between the feedback outflows and ram pressure of a comparable strength. The two short peaks in ram pressure at ∼1250 (13W) and 1700 Myr (14W) are due to shock waves generated when we stack the ram pressure profiles; they have no global effects on the simulations.

3. Global Results: Gas Stripping and SFR Response

We present our simulation results as follows: Section 3.1 summarizes the global evolution of baryonic mass, SFR, and star-forming location; Section 3.2 describes the wind-driven gas morphology and kinematics, which explains the global evolution in Section 3.1.

3.1. The Fate of the Ram Pressure Stripped Galaxy

The global effects of RPS on the disk mass and SFR are demonstrated in Figure 3, comparing the three wind cases and the iso case. The upper panel shows the galactic disk masses: gas as solid lines and gas plus formed stars as dashed lines, versus simulation time. We apply a spatial disk cut ($R_{disk} = 18$ kpc, $z_{disk} = \pm 2$ kpc) and a metallicity cut ($Z_{gas} \geqslant 0.25\,Z_\odot$) to select the gas in the galactic disk, and place the same spatial cut when calculating the masses of the formed stars. We verified that varying these selection criteria to include more gas (e.g., using $z_{disk} = \pm 5$ kpc and $Z_{gas} \geqslant 0.2\,Z_\odot$) does not change the trends. The gas fuels star formation and decreases in mass

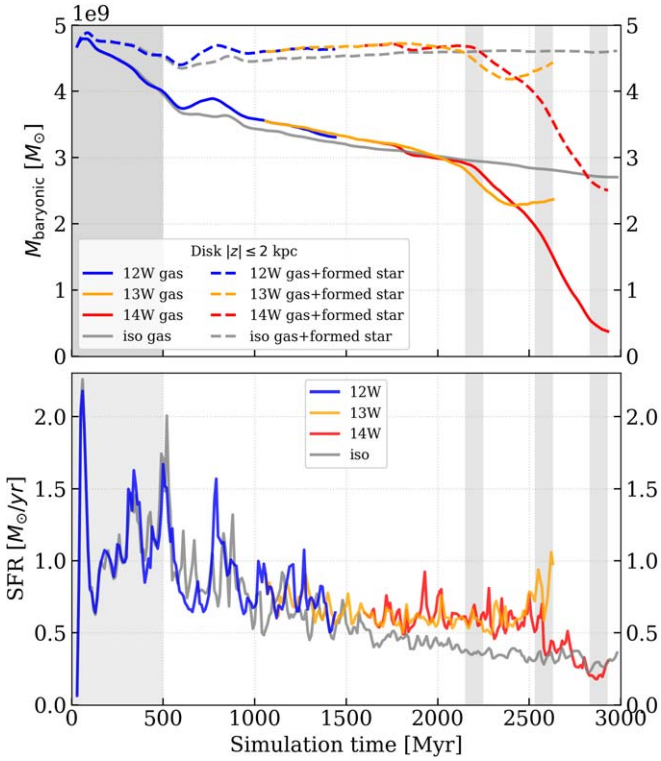

Figure 3. Upper panel: the time evolution of the galaxy disk's ISM mass (solid lines), where the ISM is specified by a combined spatial and metallicity selection (Section 3.1). The dashed lines are the ISM mass in solid lines added with the total mass of formed stars under the same spatial selection. Lower panel: the SFR time evolution. The first ∼500 Myr is the thermal relaxation phase (Section 2.3), where the disk cools and collapses, leading to an initial burst in star formation, and gradually stabilizes. This unstable phase (0–500 Myr) is shaded and will be omitted in the plots hereafter. To aid visual comparison, we denote three 100 Myr time periods with vertical bars showing the onset of effective stripping, 13W pericenter, and 14W pericenter from left to right; see Section 3.1.

in all four cases. Without RPS, star formation accounts for most of the gas mass loss, as shown by the iso case's gas plus formed stellar mass (dashed gray line), which remains at ∼98.5% of its initial value—almost conserved after ∼3 Gyr of evolution over which time nearly 45% of the initial gas mass is converted to stars.

In the wind runs, in addition to forming stars, the gas can gain or lose mass due to interactions with the wind, depending on the ram pressure strength. In 12W, there is no stripping-induced mass loss compared to the iso case due to the weak ram pressure (Figure 2). Instead, there is a mild mass excess at $t \sim 750$ Myr, because ram pressure pushes part of the feedback outflows back to the disk (this will be discussed in Section 3.2). Both 13W and 14W experience the onset of the stripping phase at $t \sim 2150$–2250 Myr, seen from the steepened gas mass slopes in Figure 3 (leftmost vertical bar; see Figure 2 for the corresponding $P_{\rm ram}$). The stripping only lasts for ∼200 Myr in 13W, after which the gas mass slope flattens as the ram pressure is kept constant (Figure 2). But in 14W, as the ram pressure continues to increase, the stripping continues until nearly the entire gas disk is removed.

The lower panel of Figure 3 shows the SFR evolution, manifesting both the SFR enhancing and quenching potential of the wind. The first ∼500 Myr is the thermal relaxation phase where star formation is still stabilizing, and the 12W wind has yet to reach the galaxy (Figure 2 and Section 2.3). This period will be omitted in subsequent plots and analyses. After the relaxation phase, the SFR steadily decreases in the iso case throughout the ∼3 Gyr of evolution, as its gas density steadily decreases due to starvation without cosmological inflow replenishing the disk. The SFR of 12W remains similar to the iso case throughout its orbit. In 13W and 14W, the SFR remains approximately constant at $\sim 0.6\,M_\odot\,{\rm yr}^{-1}$ until $t \sim 2450$ Myr, which is a relative enhancement compared with iso. The SFR then mildly increases in 13W as the gas mass remains almost constant, resulting in a 2.5 times SFR enhancement relative to iso at the first-infall pericenter (middle vertical bar). In 14W during the final 480 Myr, the SFR decreases by ∼65%, dropping to below iso at the cluster pericenter (rightmost vertical bar), as the gas is rapidly removed from the disk (from $\sim 2.2 \times 10^9\,M_\odot$ to $\sim 3.8 \times 10^8\,M_\odot$). The 14W galaxy will ultimately be quenched judging from the rapid, almost complete gas removal.

Combining the ram pressure, the disk mass, and SFR (Figures 2 and 3) gives the direct effect of ram pressure on these star-forming disks' global evolution. The turning point at $t \sim 2200$ Myr, where the effective gas stripping takes place in 13W and 14W, corresponds to a total 45° angled ram pressure of $P_{\rm ram} \approx 1.5 \times 10^{-12}$ g/(cm s^2). Before this critical ram pressure is reached, the gas plus formed stellar masses in the disks (dashed lines in Figure 3) remain conserved with respect to ram pressure for all wind runs. Unlike gas stripping, which is a direct consequence of strong ram pressure, the SFR shows no immediate correlation to ram pressure. The SFR turning points in 13W and 14W appear ∼300 Myr delayed compared to the gas mass change (Figure 3), likely because it takes time for the wind-driven mass flows around the disk to affect the global SFR.

As the wind interacts with the galactic disk, the location of star formation changes, as shown in Figure 4. We select stars newly formed within 100 Myr of each given time and obtain their distribution in cylindrical/disk radius ($R_{\rm disk}$) and height ($z_{\rm disk}$). These stars' radial distribution has a power-law tail, and Figure 4 shows their 95th percentile values as solid lines. The height distribution characterizes a thin disk of cold gas—symmetrically peaked around $z = 0$ kpc without wind impact, or skewed toward $+z$ under a wind that has a $+z$ component, and Figure 4 shows their 5th to 95th percentiles as colored bands.

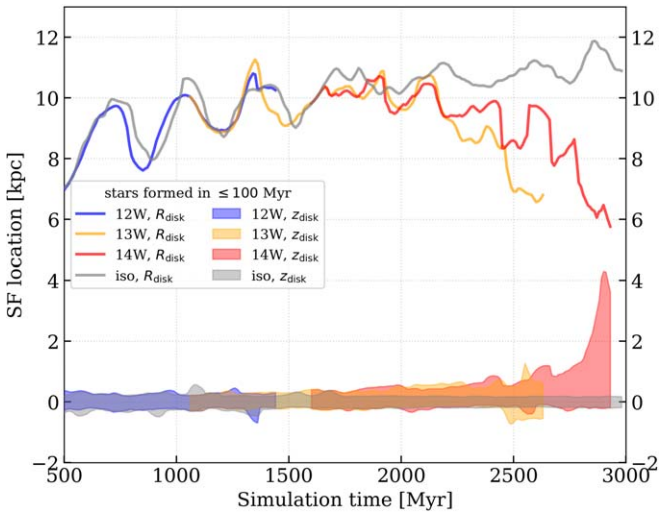

Figure 4. The evolution of star-forming locations in terms of the cylindrical/disk radius $R_{\rm disk}$ and height $z_{\rm disk}$ vs. simulation time. The radii shown here as solid lines denote the 95th percentile values, and the heights as colored bands denote the 5th to 95th percentile values. We select new stars formed within 100 Myr to match the typical timescales of UV observations (Section 3.1). Higher ram pressures lead to more central star formation.

The radial ringing in Figure 4 results from epicyclic oscillations triggered by rapid radiative cooling disturbing the initial equilibrium disk (Goldbaum et al. 2015), and has no global effect on our results. In the iso case, the radius of star formation in an undisturbed disk shows a slow and steady increase and asymptotes to ∼11 kpc at the final stage of evolution, and the height remains symmetric within ±0.5 kpc, which 12W closely follows throughout its orbit. In 13W and 14W, when the gas stripping begins at $t \sim 2200$ Myr (Figure 3), their radii of star formation begin to deviate from the iso case, with the 13W radius decreasing slightly faster and its $z_{\rm disk}$ symmetrically thickening, while the 14W radius decreasing relatively slowly to ∼6 kpc and its $z_{\rm disk}$ extending to +4 kpc, highly skewed toward the wind direction. The star formation radius in 13W decreases faster than in 14W, where ram pressure is higher, which seems to contradict the Gunn & Gott (1972) face-on stripping picture. But this is because of the wind inclination: more 14W gas is stripped into an extensive tail inclined to the disk (see Figure 5 below), forming stars in the tail, which skews the 14W star formation to higher cylindrical radii.

We selected the 100 Myr timescale in Figure 4 in order to match the typical timescales in UV observations of star formation (e.g., Kennicutt & Evans 2012; Leroy et al. 2012). We also experimented with 10 Myr (typical Hα timescale), 30 Myr, and all formed stars within the simulations (1–3 Gyr, roughly matching the timescales in optical observations, see Tasker & Bryan 2006), and found the temporal trends agree for the 10, 30, and 100 Myr selections. If using all formed stars, however, the radial distributions in all cases asymptote to $R_{\rm disk} \approx 10$–11 kpc, characterizing a steady stellar disk (rather

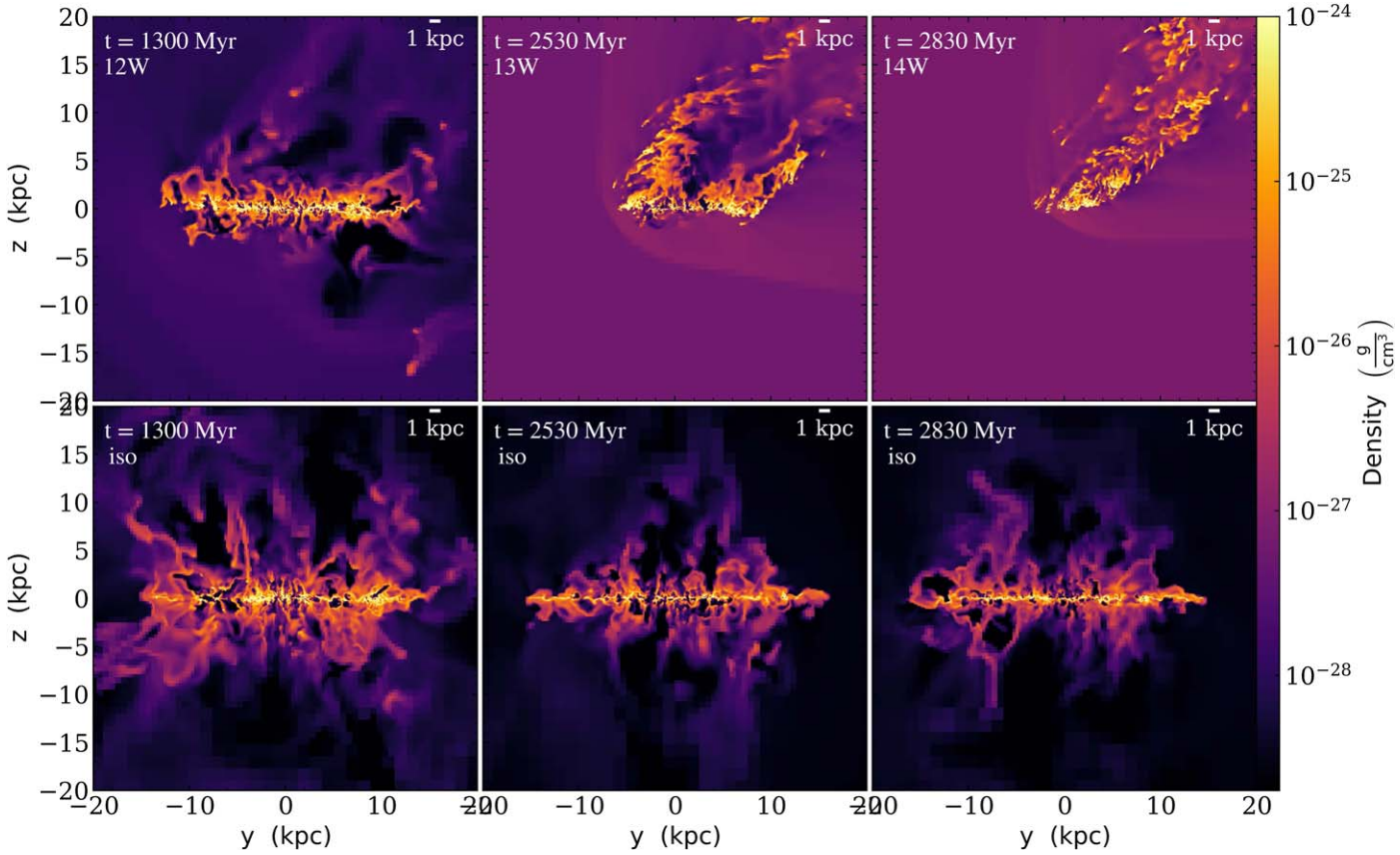

Figure 5. Gas density *edge-on* slices, zoomed in to 40 kpc. The 45° winds introduced as boundary inflows are in the $\hat{v}_{\mathrm{wind}(y,z)} = (\frac{\sqrt{2}}{2}, \frac{\sqrt{2}}{2})$ direction (Section 2.3). The selected time frames, as annotated on the upper left corners, correspond to the pericentric conditions of the 12W, 13W, and 14W orbits (Figures 2 and 3). The upper panels show the wind cases, and the lower panels show the isolated case at the same time for comparison.

than recent star formation); a similar radius across all cases is expected as RPS has no direct effect on the stellar disk.

3.2. Wind-driven Gas Morphology and Kinematics

The global results in Section 3.1 show that RPS directly affects the gas mass, and although the global SFR is eventually affected, that impact occurs a few hundred megayears after the onset of gas stripping. We find the impact on star formation can evolve in opposite directions: enhance or quench (Figure 3). In this section, we examine the wind-driven gas flows to determine the physical reasons behind the bimodal effects on star formation.

We first show the different morphology of the gas via density slices along the $x = 0$ plane in Figure 5, comparing the iso case to each wind run when the ram pressure has reached its peak value at the galaxy position. The three lower panels show that, without RPS, the isolated galactic disk remains cylindrically symmetric and drives an outflow above and below the disk via star formation feedback, which decays in strength as the SFR decreases with time (Figure 3). The three wind runs demonstrate different interactions between the wind and the galactic gas, as summarized below.

1. 12W: There is no clear signal of RPS within the gas disk. Ram pressure appears to interact with the feedback-driven outflows, likely suppressing those outflows below the disk (against the wind direction).
2. 13W: Gas is being stripped and forms an outer ring that, in this slice, looks like two tails. The feedback-launched gas below the disk in the iso and 12W runs is missing because of the higher ram pressure.
3. 14W: Gas is being stripped relatively uniformly from all radii of a shrunken and highly fragmented disk, forming a single extended tail tracing the wind direction. The 14W wind has a similar density but greater than two times higher velocity compared with 13W, leading to its greater than four times higher pericentric ram pressure (Tables 2 and 4).

Moving from 12W to 13W and finally to 14W, we see a clear progression from negligible stripping to outer gas removal to nearly complete stripping. However, the 13W gas morphology in Figure 5 demonstrates a unique complexity: within the stripping radius (characterized by the outer ring of stripped gas), there is high-density gas above the disk. We zoom in and examine the gas kinematics of 13W in Figure 6. The v_z slice (left; not mass weighted) shows that much of the gas above the disk has a $\sim$0 or negative z-velocity—falling back to the disk. The stripped material from the leading side ($y < 0$), initially traveling at 45° ($\hat{v}_{\mathrm{wind}}$), experiences gravitational forces toward the disk center where the potential well is deepest (perpendicular to the contour lines, Figure 6). This fallback phenomenon is confirmed by the mass-weighted gas velocity streamlines, indicating the paths of motion, in the edge-on projection map of gas that originated in the galaxy (middle

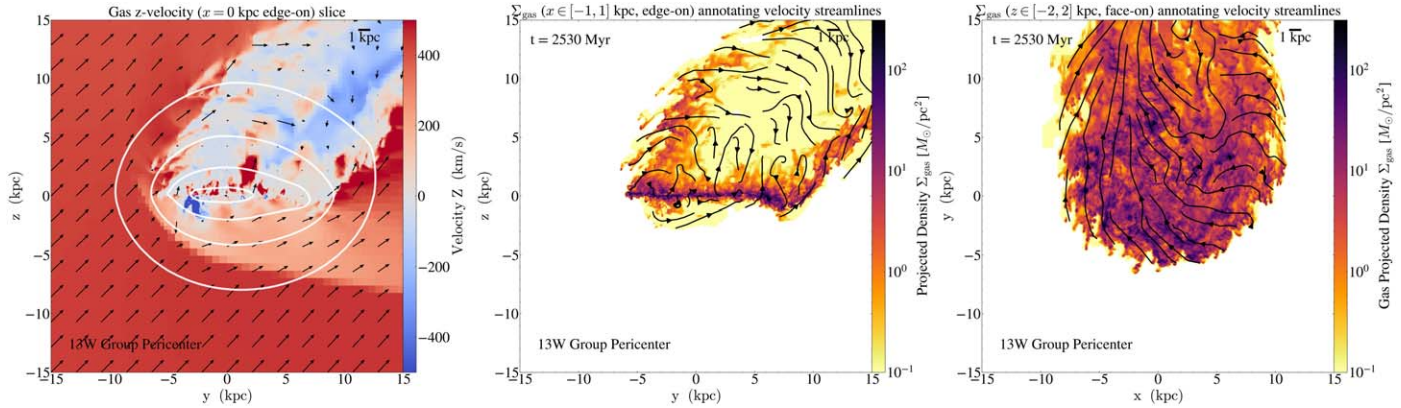

Figure 6. Gas z-velocity slice and projected density maps of 13W at the pericenter (as in Figure 5), zoomed in to 30 kpc. Left panel: gas v_z slice map, annotating gravitational potential contours in white lines. The potential includes the static stellar and dark matter components (Section 2.1), self-gravity of the gas, and of the newly formed stars. The in-plane velocity vectors ($v_{y,z}$) are marked by black arrows. Middle and right panels: gas density projection maps (edge-on and face-on) with a metallicity selection for the galactic ISM ($Z_{gas} \geqslant 0.25\ Z_\odot$; largely unmixed with the ICM). The streamlines show the mass-weighted gas velocities.

panel). Fallback happens for the relatively dense stripped gas at the wind-leading edge ($y \approx -6$ kpc) onto the leading half of the disk, and also for the more diffuse stripped gas in the tail ($z \gtrsim 5$ kpc), which occurs on a larger spatial scale.

The face-on projection map (Figure 6, right panel), on the other hand, shows the interplay between ram pressure and disk rotation within the disk plane. On the $x > 0$ side of the disk where the ram pressure in-plane component ($+y$) counters disk rotation, the disk gas can lose its angular momentum, manifested in radial inflows toward the disk center. This is clearly distinct from the $x < 0$ side, where ram pressure aligns with disk rotation, and the in-plane gas kinematics transforms into radial outflows in the wind-trailing end of the disk ($y > 0$). Gas that is pushed above the disk while losing angular momentum, as illustrated in the third panel, will be more able to fall back along the streamlines shown in the middle panel.

We now focus on RPS-driven mass losses using the gas motions perpendicular to the disk (Roediger & Brüggen 2006; Bekki 2014). In our simulations, this corresponds to flows in the z-direction, $\dot{M}_z = \int_{\rm surface} \rho\, \boldsymbol{v} \cdot d\boldsymbol{A} = \int_{\rm surface} \rho\, v_z \cdot dA_{(x,y)}$, where the surfaces are selected to be $z_{\rm disk} = \pm 2$ kpc for the gas with metallicity $Z \geqslant 0.25\ Z_\odot$,[4] consistent with our disk ISM selection (Figure 3). In addition, the mass flows are expected to have radial dependence, because gas removal typically begins at larger disk radii where the local gravity is weakest, and migrates radially inward as the ram pressure increases (Gunn & Gott 1972, also see Figure 4). To characterize the radial dependence, we further distinguish the mass flows across the full planes ($z_{\rm disk} = \pm 2$ kpc) versus only the central 5 kpc regions of the planes ($R_{\rm disk} \leqslant 5$ kpc, $z_{\rm disk} = \pm 2$ kpc). The resulting $\dot{M}_z$ of the full and central planes are shown in Figure 7, together with the gas mass and SFR time evolution (similar to Figure 3) of the central plane.

The mass-loss rates in Figure 7's left two panels are obtained by summing $\dot{M}_{{\rm gas},z}$ above and below the disk (at $z = +2$ and -2 kpc), where a positive value is outflow/mass loss by definition. For the iso case, the mass-loss rate demonstrates galactic fountain flows driven by the stochastic star formation feedback alone: in the central plane where the star formation and feedback are strongest, $\dot{M}_{{\rm gas},z}$ remains an outflow (lower left panel); but the full plane $\dot{M}_{{\rm gas},z}$ oscillates around 0 (upper left panel), and results in $\sim$0 net baryonic mass loss throughout the 3 Gyr iso simulation (gray-dashed line, Figure 3). The fountain flows' (or central plane feedback outflows') amplitudes decay as the SFR decreases with time (Figure 3). The mass-loss rate of 12W overall follows iso, except for a mildly enhanced inflow within its full plane (upper left panel) at $t \sim 600$–800 Myr, which explains the mild 12W gas mass excess around this time (Figure 3). We verified that the 12W enhanced inflow relative to iso is via the $z = -2$ kpc surface, indicating that the ram pressure, although not yet sufficient to strip the gas disk, transfers momentum with the diffuse fountain flows below the disk.

For 13W and 14W, the mass-loss rates are dominated by RPS. Across the full plane, the first peak of mass loss occurs at $t \sim 2150$–2250 Myr (leftmost vertical bar, Figure 7), corresponding to the onset of effective stripping in both 13W and 14W (Figure 3). After that, the 13W mass-loss rate steadily decreases to $\sim$0 at its pericenter, as the ram pressure becomes constant (Figure 2), and the 14W mass-loss rate keeps increasing for another $\sim$400 Myr with its still increasing ram pressure. For the central plane, however, there is a clear dichotomy: 13W shows a central inflow ($\dot{M}_{{\rm gas},z} < 0$) with increasing amplitude, while 14W shows a (slightly delayed) central outflow. During the onset of effective stripping, the stripping radius is greater than the selected central region (5 kpc), so $\dot{M}_{{\rm gas},z} \sim 0$ for both cases. At $t \sim 2500$ Myr, the 14W stripping radius reaches the inner 5 kpc, and hence the central outflows begin. But for 13W, ram pressure was never sufficient to strip the inner disk; instead, the gravitational fallback of the stripped material (as described in Figure 6) replenishes the central disk.

The right-hand two panels of Figure 7 show the central disk gas mass and SFR time evolution and the c/f ratio; see Figure 3 for the full disk). For all four simulations, the central gas mass evolution tightly correlates with the central SFR evolution. The temporal oscillations arise from the radial ringing discussed previously in Figure 4. In the absence of effective RPS, the iso and 12W cases maintain an almost constant c/f ratio throughout the simulations (gray- and blue-dashed lines). Effective RPS (13W and 14W) leads to a radial redistribution of the gas and SFR: (i) the profiles are more radially centralized (enhanced c/f ratios), and (ii) the inner disk $M_{\rm gas}$ and SFR values (solid lines) are both enhanced relative to iso. Although (i) partially results from the removal of outer disk gas, (ii)

[4] The metallicity selection excludes the ICM inflows (Section 2.3).

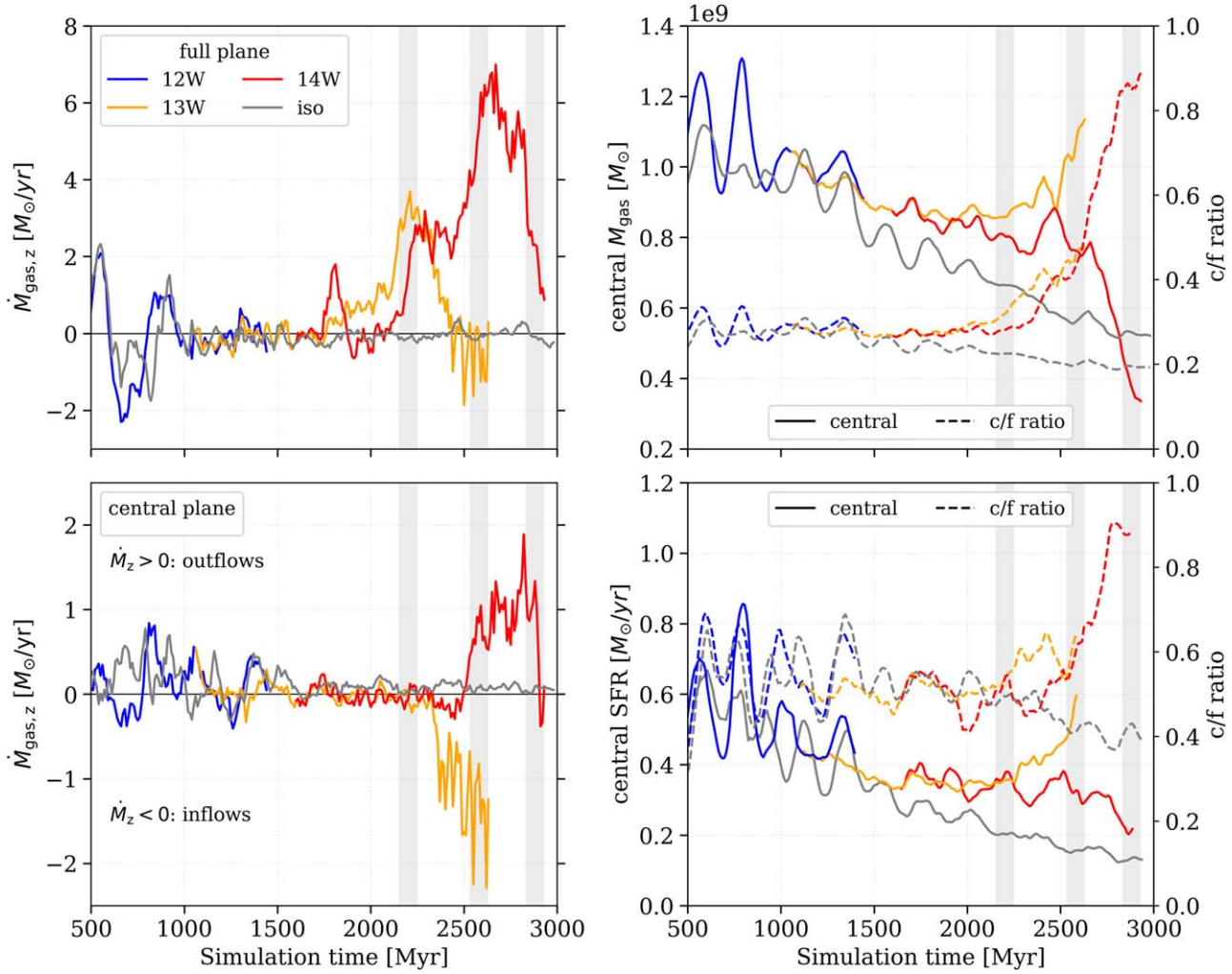

Figure 7. Left: gas mass-loss rate perpendicular to the disk ($\dot{M}_{gas,z}$, where positive values indicate outflows), evaluated at disk heights $z = \pm 2$ kpc, for the full plane (upper left) and the central 5 kpc regions (lower left). Right: the central 5 kpc gas mass (upper right) and SFR (lower right) time evolution as solid lines (similar to Figure 3, here for the central disk), and the central-to-full disk ratio (c/f ratio) as dashed lines on the right-hand y-axes. In all panels, we show the three 100 Myr reference time frames as in Figure 3.

directly reflects the star formation enhancement potential of RPS.

The gas motions perpendicular to the disk (Figure 7) demonstrated an indirect mode of radial mass transfer in 13W: gas is lifted by RPS from the edge of the disk, and falls back to the central disk a few 100 Myr later, replenishing star formation there (also see Figure 6, middle panel). Another mode of radial mass transfer is directly via the (cylindrical) radial direction, $\dot{M}_\varpi = \int_{\rm surface} \rho\, \boldsymbol{v} \cdot d\boldsymbol{A} = \int_{\rm surface} \rho\, v_\varpi\, dA$, where $\hat{\varpi}$ is the cylindrical radial vector, and the surface can be approximated by a thin cylindrical shell of average width $\bar{h}$, such that $\dot{M}_\varpi \approx (1/\bar{h}) \sum_i^{\rm shell} (m_i\, v_{\varpi,i})$. We evaluated the radial mass flow rate for the central disk in Figure 8 ($R_{\rm disk} \leqslant 5$ kpc, $|z_{\rm disk}| \leqslant 2$ kpc).[5] Because $\dot{M}_\varpi$ characterizes mass transfer within the galaxy, its amplitude is particularly susceptible to radial oscillations (Figure 4). Therefore, we show the time cumulative ($\Delta M = \sum \dot{M}(t)\, \Delta t$; frequent temporal oscillations cancel out) mass flows in Figure 8: the left panel compares the radial and vertical (perpendicular to the disk) components, the right shows the total kinetic flows (the sum of the two).

The dashed lines in the left panel of Figure 8 represent the time integration of the central plane $\dot{M}_{gas,z}$ (Figure 7 lower left panel). As described above, in the central plane there is a consistent feedback outflow in iso, fallback replenishment in 13W, and stripping in 14W when $P_{\rm ram}$ becomes sufficient to affect the inner disk ($R_{\rm disk} \leqslant 5$ kpc). In the radial direction (solid lines, Figure 8 left panel), however, both 13W and 14W show an excess of inflow relative to iso, with peak amplitudes ($\Delta M_{\rm inflow} \approx 2 \times 10^8\, M_\odot$) comparable to the net fallback inflow in 13W. These radial inflows can be explained by an interplay between the edge-on ram pressure component and disk rotation (right panel of Figure 6). Rotating gas in the disk, when countered by ram pressure (where $x > 0$; Figure 6), can lose angular momentum and migrate radially inward. For 14W, this radial inflow eventually decreases to 0 as stripping proceeds into the central region of the disk with increasing $P_{\rm ram}$.

The right panel of Figure 8 shows the sum of the radial and vertical components: the total kinetic mass transport across all surfaces of the central disk. We summarize the key physical

[5] The shell width $\bar{h}$ is obtained by $\bar{h} = (1/A_{\rm shell}) \sum_i^{\rm shell} V_i$, where V_i is the individual cell volume, and $A_{\rm shell} = 2\pi R_{\rm disk} \cdot (2 z_{\rm disk})$ is the shell area. We tested a range of shell widths, $\bar{h} \in [39, 156]$ pc, which corresponds to one to four times the highest refined cell length (Section 2), and $\dot{M}_\varpi$ is approximately constant over these $\bar{h}$. After obtaining $\bar{h}$, we evaluate $\dot{M}_\varpi(\bar{h})$ for the cells in the thin shell that satisfy the ISM metallicity selection $Z \geqslant 0.25\, Z_\odot$. The final $\dot{M}_\varpi$ is an average of $\dot{M}_\varpi(\bar{h})$ over $\bar{h} \in [39, 156]$ pc.

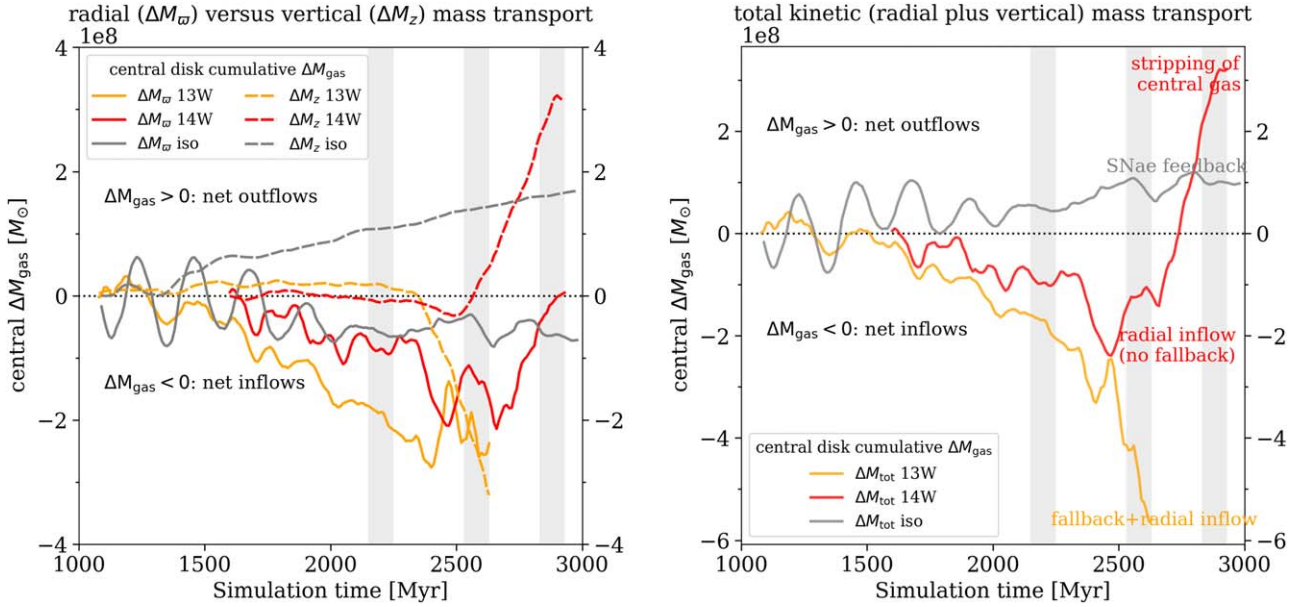

Figure 8. The cumulative mass loss (ΔM_{gas}) over time for the central 5 kpc disk as driven by mass transport, comparing 13W, 14W, and iso. Left: the cylindrical radial (ΔM_ϖ; solid lines) vs. vertical (ΔM_z; see Figure 7 for $\dot{M}_z$, here dashed lines) mass-loss components. Right: the total kinetic mass loss by summing the two components. As in Figure 7, positive ΔM_{gas} values denote outflows, and the vertical bars show the three reference time frames. Key physical processes that explain the trends are annotated on the right panel.

processes at play in the figure. For iso, the gradual mass loss is dominated by the central plane's star formation feedback. For 13W, there is a combination of replenishment from fallback and from direct radial inflow, resulting in its highest central plane gas mass and SFR (Figure 7 right panels). For 14W, because the ram pressure keeps increasing, there is net replenishment from radial inflow but little to no fallback around the group pericentric time (middle vertical bar), which eventually becomes a net outflow as the stripping radius reaches within the selected central disk ($R_{disk} = 5$ kpc) at the cluster pericenter (rightmost vertical bar). Collectively, the kinetic mass transport (Figure 8) explains the central plane M_{gas} and SFR evolution (Figure 7). We found RPS-driven direct radial inflows, in agreement with literature results (Schulz & Struck 2001; Tonnesen & Bryan 2009; Akerman et al. 2023), can replenish the central star-forming disk; and we identified fallback as an indirect mode of radial mass transport (Figures 6–8) that can add to the enhancement for certain orbits.

We emphasize that as long as the $P_{ram}(t)$ profiles are consistent, even with different ρ_{ICM}, v_{sat} components (Section 2.3), the galaxy undergoes a similar global evolution. For example, at $t \sim 2200$ Myr (leftmost vertical bar), the global properties and the mass-loss rates of 13W and 14W closely match (Figures 3, 7, and 8) as their P_{ram} values are comparable (Figure 2), despite the 14W orbit consisting of a higher v_{sat} and a lower ρ_{ICM}. Importantly, the galaxy's global evolution is also sensitive to the time derivative of ram pressure, dP_{ram}/dt. When the 13W ram pressure stops increasing as the galaxy reaches the group pericenter ($dP_{ram}/dt = 0$, Figure 2 leftmost to middle vertical bar), the stripping radius is kept constant and the remaining gas disk acts as a *shield* for the stripped gas above it, such that gravity outweighs ram pressure in shielded regions and causes the central plane fallback ($\dot{M}_z$, Figure 7). Conversely, in 14W where dP_{ram}/dt keeps increasing after $t \sim 2200$ Myr for ~500 Myr, the stripping radius decreases, so the shielded region shrinks (Figure 5); without shielding the stripped gas above the disk is unable to fall back.

The global evolution described in Sections 3.1 and 3.2 can be summarized as follows. In the iso run, the gas disk primarily loses mass to steady star formation, which drives feedback fountain flows that decrease in magnitude with decreasing SFR. In 12W with weak P_{ram}, the global properties are overall consistent with iso, other than the additional interactions between the wind and the low-density fountain flows. In 13W with moderate P_{ram}, RPS in the disk outskirts dominates the mass loss, and actually enhances the SFR in the remaining disk. Because the pericentric P_{ram} is insufficient to remove the entire gas disk, gas can migrate radially inward via fallback and direct radial inflows, both replenishing the central disk's star formation. In 14W, P_{ram} is sufficient to strip the gas first in the outskirts and then in the center, ultimately resulting in a rapid decline in the galaxy's SFR.

4. Spatially Resolved SFR–Mass Relation

In the previous section, we found that RPS can enhance the satellite galaxy's global SFR while removing its gas (Figure 3), and the wind-enhanced star formation favors central disk regions (Figures 4 and 7). In this section, we evaluate the spatially resolved SFR–mass relations—a direct clue to the star formation microphysics (e.g., Kennicutt & Evans 2012). We compare the relations between the RPS and isolated cases to characterize the physical conditions of ram-pressure-enhanced star formation.

4.1. Spatial Division Methodology and Radial Profiles

When spatially resolving galactic regions, the sampling scales need to exceed certain minima for galactic star formation–mass scaling relations to hold (Kruijssen & Longmore 2014; Kruijssen et al. 2018); the selected sampling scales need to account for the incomplete statistical sampling of independent star-forming regions and the spatial drift between

Table 5
Summary of the 1 kpc^2 Patch Selection

Case	t_{peri} (Myr)	$N_{patch,SF}$	SFR_{global} ($M_\odot$ yr^{-1})	τ_{dep} (Gyr)
(1)	(2)	(3)	(4)	(5)
13W pericenter	2530–2630	1427	0.85	2.28
iso group control	2530–2630	3016	0.38	7.12
14W pericenter	2830–2930	447	0.21	1.70
iso cluster control	2830–2930	2933	0.32	8.16
iso pre-starvation	580–680 (a)	2292	1.08	3.11

Note. Column (1) Simulation cases. Column (2) Simulation time periods that correspond to 13W and 14W pericenter passages. (a) The iso *pre-starvation* time frame is selected to match the central plane M_{gas} of the 13W pericenter (Figure 7), see Section 4.1. Column (3) The number of star-forming patches, where star formation is defined to have $\Sigma_{SFR} > 10^{-6}\,M_\odot/(\mathrm{yr\,kpc^2})$ per patch. Column (4) The total SFR of the star-forming patches averaged over the selected 100 Myr time period. Column (5) The gas depletion time defined as $\tau_{dep} = M_{gas}/\mathrm{SFR}$, where M_{gas} is the total gas mass in the patches, and SFR is as in Column (4).

gas and stars. Empirically, this minimum spatial scale Δx works out to be ∼1 kpc for typical star-forming galaxy disks (see Kruijssen & Longmore 2014, Figure 2). Here, we select the sampling scale to be 1 kpc^2 to satisfy the validity of the scaling relations; and to match with typical scales (0.75–1.2 kpc^2) in high-angular-resolution observations in the local universe (Bigiel et al. 2008; Vulcani et al. 2019, 2020; Jiménez-Donaire et al. 2023).

For a given simulation snapshot, we divide the satellite disk into 1 kpc^2 resolved patches, integrate the patches along the disk height direction (for disk height $|z| \leqslant 2$ kpc), and calculate the projected SFR, gas, and stellar surface densities (Σ_{SFR}, Σ_{gas}, and Σ_*) of each patch. We focus on the galaxy group and cluster pericenter time frames, when RPS most effectively enhances/quenches the satellite star formation (Figure 3), and compare the wind cases with the isolated galaxy case (iso) at the corresponding times. Using 100 Myr windows (10 simulation outputs) produces larger samples of 1 kpc^2 regions with recent star formation (10 Myr) across the disk. Changing the number of outputs does not qualitatively affect our results. The global properties of the selected patches are summarized in Table 5. Throughout the section, we will focus on the four pericentric cases in Table 5: 13W, 14W, iso group, and iso cluster control, while iso pre-starvation is a special reference case for the star formation law comparison in Section 4.2 below.

The radial profiles of the resulting patches are shown in Figure 9. The SFR profiles (top panel) closely resemble the respective gas profiles (bottom panel) in all cases. In the central few kiloparsecs, the wind cases (blue) are enhanced in both the SFR and gas densities relative to iso (red); at larger radii, the wind radial profiles show a steeper decrease with radius than iso. This is expected given our previous finding that ram pressure removes gas in the outer disk while driving gas into the central disk (Figure 7). The 95% enclosing radii of the SFR, denoted by the open circles, show that star formation is more centrally concentrated with increasing ram pressure, with the iso cases forming stars within ∼9.0 kpc (no ram pressure), 13W within ∼5.4 kpc (moderate ram pressure, enhanced SFR), and 14W within ∼2.3 kpc (strong ram pressure, approaching complete stripping). The time evolution in iso from the group to cluster pericenter times (∼300 Myr duration; red solid and dashed curves) is due to star formation *starvation*, which has a relatively small impact on the radial profiles (and reduces the global SFR by ∼16%; see Table 5).

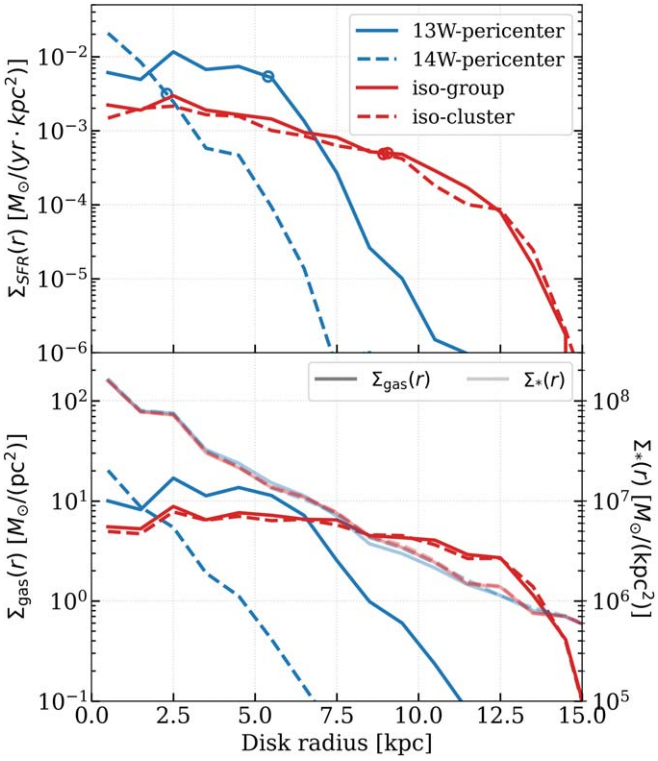

Figure 9. The SFR, gas, and stellar surface densities (Σ_{SFR}, Σ_{gas}, and Σ_*) radial profiles of the resolved 1 kpc^2 patches. The four cases (Table 5) are 13W and 14W at pericenters (solid and dashed in blue) and iso group and cluster control cases (same line styles in red). In the top panel, the open circles show the radii enclosing 95% of the Σ_{SFR}. In the bottom panel, Σ_{gas} (deeper colors; left-hand y-axis) and Σ_* (lighter colors; right-hand y-axis) are shown under the same scale, following the conventional units of each quantity.

The bottom panel of Figure 9 directly compares the gas and stellar surface density (Σ_{gas} and Σ_*) profiles. The y-axes are under the same physical scale following the conventional units of each quantity, as will be used in Sections 4.2 and 4.3 and the figures therein. In all cases, Σ_* profiles (lighter lines) are greater than Σ_{gas} (deeper lines) within the inner ∼8 kpc region that encloses the majority of star formation. Unlike Σ_{gas} (or Σ_{SFR}), which clearly distinguishes wind and iso, the Σ_* profiles are consistent among all cases. This is because (i) ram pressure only directly impacts the gas disk and not the stellar disk; (ii) the formed stellar mass is low compared with the static stellar potential ($\Delta M_{\mathrm{formed\ star}}/M_{\mathrm{static\ disk}} < 3\%$; Figure 3 and Section 2); therefore, the total Σ_* is dominated by the static stellar potential at all radii.

4.2. SFR–M$_{gas}$: The Kennicutt–Schmidt Relation

We investigate the SFR–M_{gas} relation, also known as the Kennicutt–Schmidt (KS) relation (Schmidt 1959; Kennicutt 1989), for the resolved 1 kpc^2 patches. The KS relation is an empirical power law between the observed SFR and gas surface densities, $\Sigma_{SFR} = A \cdot \Sigma_{gas}^N$. Physically, it is a proxy for how efficiently gas forms stars at given surface densities. In our suite of simulations, both the stripping and the isolated galaxy cases follow the same numerical star formation and feedback recipe (Goldbaum et al. 2015, 2016; see Section 2), and

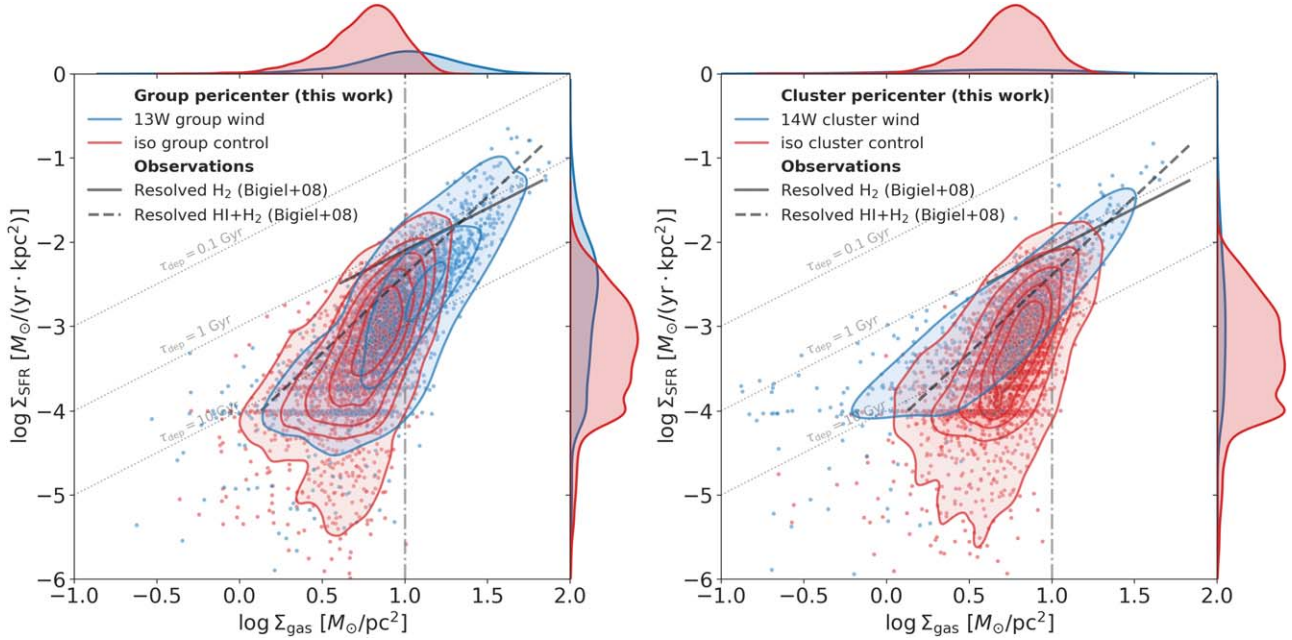

Figure 10. Spatially resolved SFR–M_{gas} (Σ_{SFR}–Σ_{gas}; KS) relation within disk height $|z| \leqslant 2$ kpc. The left and right panels show the 100 Myr duration of the galaxy group and cluster pericentric passages (or the corresponding times in iso; Table 5), respectively. Each panel shows the Σ_{SFR}–Σ_{gas} bivariate and one-dimensional (1D) distributions of 1 kpc^2 patches in the iso (red) and wind (blue) simulations. Solid and dashed black lines show the spatially resolved KS power law from Bigiel et al. (2008) over the observed Σ_{gas} ranges for H_2 and H I+H_2 combined, see Section 4.2 for details. Constant depletion time contours $t_{dep} = 0.1$, 1, 10 Gyr are annotated in gray-dotted lines. The gray vertical line indicates the atomic-to-molecular gas density transition at $\Sigma_{gas} \approx 10\ M_\odot\ pc^{-2}$ (Krumholz et al. 2009).

differences on the Σ_{SFR}–Σ_{gas} (KS) phase plane will directly reflect the impact of RPS.

Figure 10 shows the KS relation in the RPS and isolated galaxy disks at the group and cluster pericenters (Table 5). For all cases, the gas densities are tightly correlated with SFR on the resolved scale, but the RPS cases populate a distinct phase space of high-density, high-SFR gas that is absent in iso. To quantify this excess, we first identify the 99.85 percentile surface density thresholds (empirically 3σ upper limits) in iso using the 1D histograms of Σ_{SFR} and Σ_{gas}. For each of these distributions, these upper limits are nearly identical at both the group and cluster pericentric times: $\log \Sigma_{gas}/(M_\odot\ pc^{-2}) \gtrsim 1.2$ and $\log \Sigma_{SFR}/(M_\odot\ yr^{-1}\ kpc^{-2}) \gtrsim -1.8$. Many patches in 13W and 14W occupy the KS phase space beyond these upper limits in iso (blue scatter points; upper right corner of Figure 9); these are the dense gas excess in the RPS cases and have a significant contribution to the total SFR (~58% in both 13W and 14W).

For 13W, star formation from this dense gas (58% or $0.5\ M_\odot\ yr^{-1}$) is comparable to its SFR enhancement relative to iso ($\Delta SFR_{group} \approx 0.45\ M_\odot\ yr^{-1}$; Table 5). For 14W, ram pressure is strong enough to remove most of the surviving ISM and leads, ultimately, to a quenching of star formation. Despite 14W's dense gas excess, its number of star-forming patches ($N_{patch,SF}$; Table 5) has decreased to ~30% of 13W and ~15% of the iso control, resulting in its lowest total SFR of all cases. We will further discuss why gas and SFR surface densities are enhanced in the RPS cases in Section 5.1.

We showed in Figure 10 that the RPS and iso cases populate different Σ_{gas} ranges. At the selected pericentric time frames, Σ_{gas} in iso primarily belongs in the H I-dominated regime (the left of the dashed vertical line in both panels), while in 13W and 14W, it populates both H I and H_2 regimes (Krumholz et al. 2009). The relatively low surface densities in iso are a direct result of the gradual gas consumption due to star formation and the feedback-driven outflows, also known as *starvation* (Larson et al. 1980; van den Bosch et al. 2008; Trussler et al. 2020). To evaluate the effect of RPS on the KS relation over a similar Σ_{gas} range, we identified an earlier time frame in iso (iso pre-starvation; see Table 5), where the central disk gas mass—and hence the highest Σ_{gas}—is comparable to 13W at the pericenter (Figure 7). This comparison will determine if the star formation efficiency at given gas densities is modified in the RPS cases.

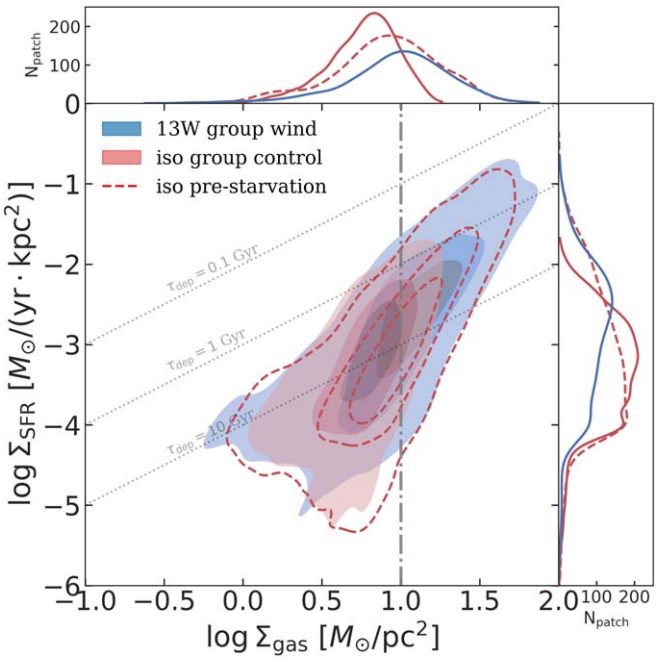

Figure 11. The effects of RPS vs. starvation on the KS plane. The red- and blue-filled contours and solid 1D distribution lines represent iso group control and 13W pericenter, respectively (as in Figure 10), and the red-dashed lines are for iso at an earlier time (prior to ~2 Gyr of starvation; see Section 4.2). The constant depletion time contours are shown as in Figure 10.

Figure 11 shows the effect of RPS versus starvation on the KS plane by comparing three cases: 13W and iso at group pericenter time and iso pre-starvation. Starvation shifts the isolated galaxy to lower surface densities along the KS relation (red-dashed versus red-filled line) via gas consumption and feedback-driven outflows. However, the iso pre-starvation case shares a very similar KS relation with the RPS case (red-dashed versus blue-filled line), despite their distinct evolutionary history and gas morphology (Figures 3 and 5). Judging from the similar KS relation, the star formation efficiency in RPS and iso cases remains the same at comparable $\Sigma_{\rm gas}$.

Independent of RPS, the resolved patches in our simulations show a KS power-law slope turnover from the H I to H_2 regimes when sufficient dense gas exists as H_2 (Figures 10 and 11). This is a direct reflection of our numerical star formation recipe (see Goldbaum et al. 2016, Figure 5), which agrees with observational findings that the KS power-law slope transitions from superlinear in the atomic regime ($N_{\rm KS,H\,I} > 1$ with poor correlation; Bigiel et al. 2008; Leroy et al. 2008; Kennicutt & Evans 2012) to approximately linear in the molecular regime ($N_{\rm KS,H_2} \approx 1$; Krumholz et al. 2009, 2012; Heiderman et al. 2010; Jiménez-Donaire et al. 2023; see the solid line in Figure 10). We also annotated the H I+H_2 combined fitting result from Bigiel et al. (2008) in Figure 10 (dashed line, $N_{\rm KS} \approx 1.8$); our simulations follow a mildly steeper slope in the atomic regime ($N_{\rm KS,H\,I} \approx 2.0$), still well within the observational scatter (Bigiel et al. 2008). An exception to the overall consistent KS slope in our simulations is 14W at the lowest gas surface densities ($\Sigma_{\rm gas} \leqslant 0$ $M_\odot\,{\rm pc}^{-2}$; see Figure 10, right panel), which shows distinctively higher $\Sigma_{\rm SFR}$ than iso and hence a lower KS slope in the low-density H I regime. The high $\Sigma_{\rm gas}$ (H_2-dominated) regime in 14W is similar to the other cases. We suspect that the low-density star-forming gas in 14W is driven by fast gas removal from RPS in recently star-forming regions.

4.3. SFR–M_*: Strong Stripping and Disk Truncation

In this section, we investigate the SFR–M_* relation, also known as the star formation main sequence relation (e.g., Schiminovich et al. 2007; Sargent et al. 2014; Speagle et al. 2014), on the spatially resolved $\Sigma_{\rm SFR}$–Σ_* plane. We examine the impact of RPS using our simulations and make comparisons with Vulcani et al. (2020; from the GAs Stripping Phenomena in galaxies "GASP" survey; Poggianti et al. 2017). The SFR surface densities of the resolved simulation patches are identical to those in the KS relation (Section 4.2), while the stellar surface densities are a combination of the static stellar disk and the formed star particles as outlined in Section 4.1, which turns out to be highly consistent among all simulations (Figure 9). The Vulcani et al. (2020) sample contains $\sim$1 kpc^2 resolved patches within 30 RPS galaxies under various stripping stages in nearby clusters, along with 10 isolated control case galaxies of similar masses (see Vulcani et al. 2019). Our simulated galaxy with $M_* \approx 10^{9.8}\,M_\odot$ lies well within the GASP sample range and is directly comparable.

Figure 12 shows the $\Sigma_{\rm SFR}$–Σ_* relation for the resolved patches, comparing 13W and 14W at their pericenters with the respective iso control cases in the same style as Figure 10. Since Σ_* is a tight, monotonic function of disk radius (Figure 9), it is an indicator for star formation location on the $\Sigma_{\rm SFR}$–Σ_* phase plane. Two major effects of RPS can be identified from the differences between the wind and iso cases, (i) the truncation of the star-forming disk, shown by the high-Σ_* cutoffs for star formation, $\Sigma_* \approx 10^{6.5}(M_\odot\ {\rm kpc}^{-2})$ in 13W and $10^7(M_\odot\ {\rm kpc}^{-2})$ in 14W; (ii) the enhancement of star formation in the central disk regions, shown by the $\Sigma_{\rm SFR}$ excess at $\Sigma_* \gtrsim 10^{7.1}(M_\odot\ {\rm kpc}^{-2})$ in 13W and $\Sigma_* \gtrsim 10^{7.6}(M_\odot\ {\rm kpc}^{-2})$ in 14W. The disk truncation is more evident in 14W, where the ram pressure is higher, which is consistent with the radial profiles (Figure 9).

In Figure 12, we annotated the GASP best-fit power-law lines for the stripping (solid) and isolated control (dashed lines) samples (Vulcani et al. 2020), where the slopes are almost identical, but the stripping sample is $\sim$0.35 dex higher in $\Sigma_{\rm SFR}$ at all Σ_*. Our result is consistent with Vulcani et al. (2020) at high Σ_* (central disk regions) that the spatially resolved SFR is enhanced in the stripping cases. But we do not see a similar SFR enhancement at low Σ_*; instead, the low-Σ_* phase space is poorly populated in our wind cases due to disk truncation. We note that, however, the Vulcani et al. (2020) sample contains an ensemble of galaxies with a range of M_*, inclinations, and environments, while our simulations focus on one galaxy under different ram pressure strengths versus in isolation. The disk truncation and SFR enhancement in our wind cases are consistent with the "Jstage=3" (strongest stripping) galaxies in Vulcani et al. (2020), which do have a steeper fitted $\Sigma_{\rm SFR}$–Σ_* slope.

We also examined earlier pre-pericenter time frames in our simulations: qualitatively, the wind cases at earlier times (weaker stripping) show a similar truncation at the lowest Σ_* (disk edge) and a mild SFR enhancement at relatively high Σ_* as those in Figure 12. The transition Σ_*, where $\Sigma_{\rm SFR}$ in the wind cases becomes higher than in iso, increases with ram pressure strength, as expected for outside-in stripping. We will present the *time-stacked* results from various RPS stages in Section 5.2.

5. Discussion

5.1. Impacts of RPS on Star Formation

Our key results in Sections 3 and 4 are,

1. In certain orbits, RPS can lead to an enhanced global SFR in relatively gas-deficient galaxies.
2. The SFR enhancement is driven by an excess of dense gas in the disk central regions, while the star formation efficiency at given gas surface densities (the KS relation) remains the same.

There are two possible channels through which the SFR is enhanced in the galaxies undergoing RPS: compression and mass transport, which are usually not separable (Tonnesen & Bryan 2012; Roediger et al. 2014; Troncoso-Iribarren et al. 2020; Vulcani et al. 2020). The ISM at the ram pressure interface can be locally compressed, leading to a higher SFR and efficiency; global mass flows driven by ram pressure can redistribute gas in the disk and cause SFR enhancement.

Our results show that RPS-driven mass transport, including fallback and radial inflows (Section 3.2; Figures 7 and 8), is directly responsible for the central disk gas mass enhancement relative to iso during the approximately gigayear early stripping stage (Figure 7 upper-right panel). The centralized ISM mass distribution in the RPS galaxies results in enhanced central surface densities ($\Sigma_{\rm gas}$ and $\Sigma_{\rm SFR}$; Figures 9 and 10), which account for the global enhancement of SFR in the stripping

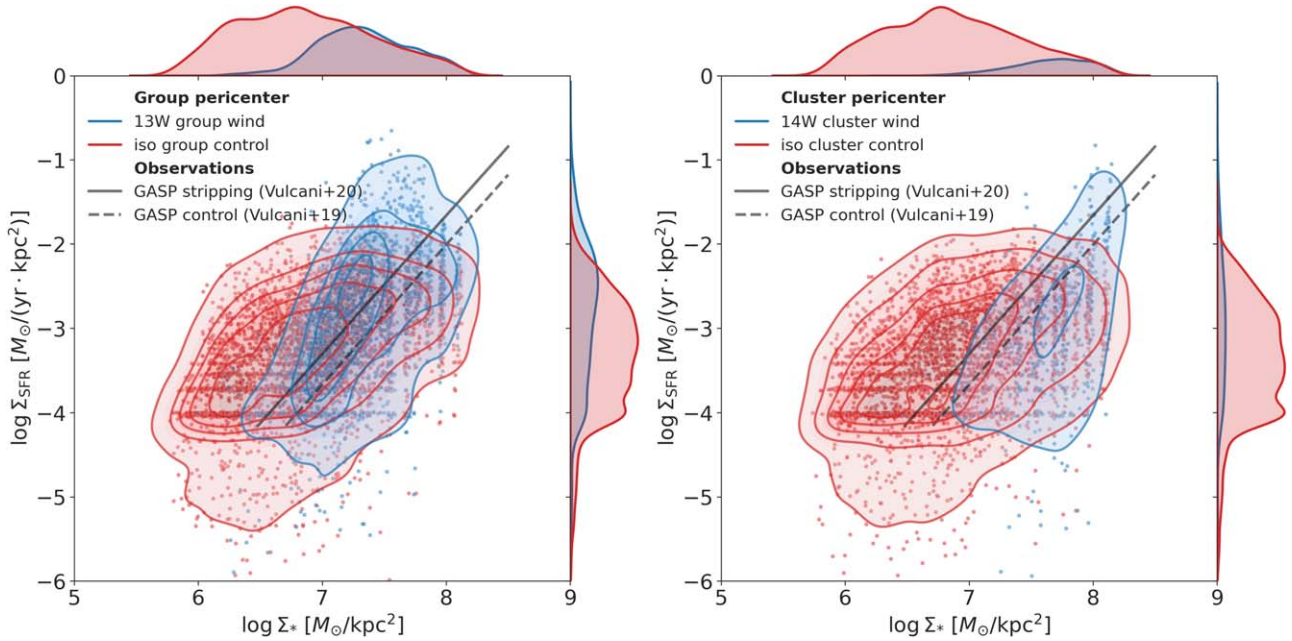

Figure 12. Spatially resolved SFR–M_* ($\Sigma_{\rm SFR}$–Σ_*) relation within disk height $|z| \leqslant 2$ kpc, in the same style as Figure 10. The stellar surface densities are a combination of the static Plummer–Kuzmin potential (Section 2.1 and Table 1) and the formed stars (as active particles) in the simulations. The black lines show the best-fit relations for the GASP stripping (solid; Vulcani et al. 2020) and isolated control (dashed lines; Vulcani et al. 2019) samples; both relations are shown over the observed $\Sigma_{\rm SFR}$, Σ_* ranges, see Vulcani et al. (2020).

cases relative to iso (with only starvation). The signal of relative SFR enhancement exists for longer than gigayear timescales unless ram pressure becomes sufficient to remove the entire gas disk and quench the star formation (Figure 3).

The role of compression is more challenging to quantify and is often inferred indirectly. Roediger et al. (2014) found that compression, indicated by shock passages, can drive a local, short-lived SFR burst (∼15 Myr), but it only impacts the low-density outer disk and only has a mild effect on the global SFR. Choi et al. (2022) modeled a local patch of star-forming galactic disks under RPS and found a similar short-lived enhancement (∼20 Myr; see their Figure 13(c)) in the dense gas surface density ($\Sigma_{{\rm gas},n_{\rm H}>10\,{\rm cm^{-3}}}$), demonstrating vertical gas compression by the initial ram pressure passage. Compression would increase the gas volume density ($\rho_{\rm gas}$) without increasing the surface density integrated throughout the disk ($\Sigma_{\rm gas}$). If such compression happens, at comparable $\Sigma_{\rm gas}$, $\Sigma_{\rm SFR}$ will be systematically higher on the KS plane. However, our Figures 10 and 11 show that at the same gas surface densities, the stripping set follows the same KS relation as the iso set. This suggests that local compression is insufficient to account for the galaxy-scale SFR enhancement in our simulations.

Another search for compression in RPS galaxies in simulations was performed by Troncoso-Iribarren et al. (2020), which spatially divided satellite galaxy disks from the EAGLE simulations into leading and trailing halves (LH and TH) separated by the infall velocity vector. Under this LH-TH division, which maximizes the SFR asymmetry between the two halves of the satellite galaxies, Troncoso-Iribarren et al. (2020) found that gas in the LH that tends to be more compressed, as inferred from higher average pressure, also has a higher star formation efficiency (defined as the total SFR/$M_{\rm gas}$) compared with the TH. Here, we follow the methodology of Troncoso-Iribarren et al. (2020) to further test for galaxy-scale effects of compression. We divide the galaxy disks based on a simple LH: $y < 0$ and TH: $y \geqslant 0$ spatial criterion, given the infall velocity vector (Figure 5) and that the star-forming disk is thin throughout the simulations (Figure 4). In the discussion hereafter, we will assume that the LH is under higher compression than the TH because of ram pressure. The disparity (or the lack of) in mass and star formation between the LH and TH will help disentangle the effects of mass transport and compression.

Figure 13 shows the SFR and gas radial profiles of the wind and iso runs (similar to Figure 9), distinguishing the LH (solid lines) and TH (dashed lines) of the disks. As expected, the surface density profiles for the isolated galaxy control case are an equal division between the two halves at all radii. In the wind runs, the surface densities in the LH consistently show a steeper decrease with disk radius than the TH; the disk radius at which the two halves diverge decreases with ram pressure. The more extended low $\Sigma_{\rm SFR}$, $\Sigma_{\rm gas}$ material in the TH is caused by the asymmetric disk morphology[6] under an inclined wind (Figure 5). Within the central few kiloparsecs of the disk, the surface density profiles show a mild LH excess in 13W and a stronger excess in 14W. However, we found that the 14W signal oscillates over time,[7] which is likely due to the orbit of the few dense clouds remaining before complete stripping instead of compression.

Figure 14 shows the time evolution of the LH-TH disparity. The time-dependent differences in the SFR and gas mass are subject to oscillations due to disk rotation and epicyclic motions (as previously shown in Figure 4; also see Tonnesen & Bryan 2009), which always average to ∼0 in the absence of

[6] Our $|z| \leqslant 2$ kpc disk height selection excludes tail contamination.

[7] Figure 14 shows the temporal oscillations of the LH-TH differences, which can explain the 14W central disk LH excess in Figure 13. If we select, e.g., 100 Myr prior to the pericenter (t = 2730–2830 Myr), the LH densities become lower than the TH in the central disk. But the mild LH excess in the 13W central disk is independent of the oscillations during the few hundred megayears approaching the pericenter because the accumulation of fallback gas mildly favors the LH (Figure 6).

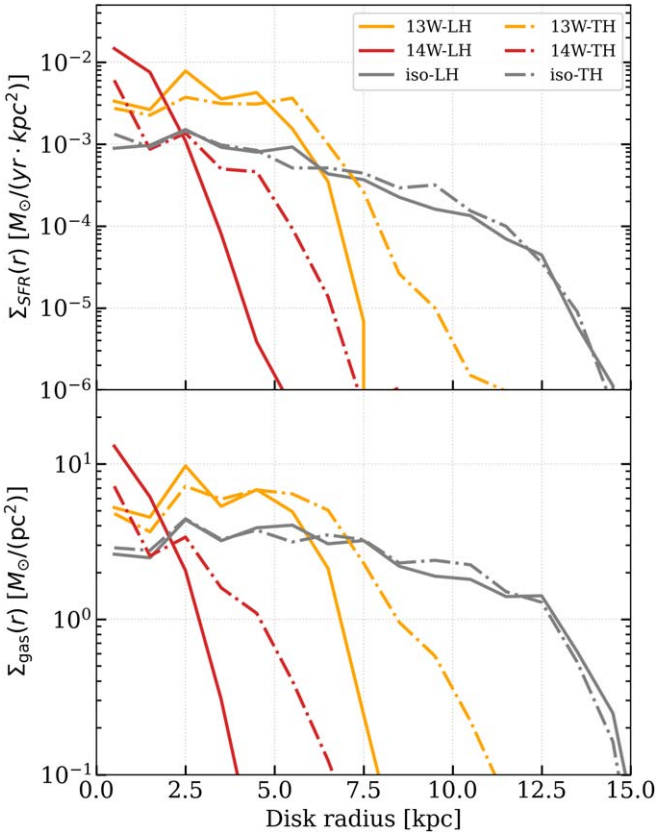

Figure 13. The SFR and gas surface density radial profiles (described in Section 4.1) for the wind LH and TH of the disks. The simulations are color coded as in Section 3, and we omitted 12W where the ram pressure has negligible impacts on the gas or SFR (Figure 3). For each wind simulation, we averaged over the 100 Myr closest to the pericenter (10 outputs), as in Table 5; for iso, we selected the group pericenter time, which yields a largely consistent profile with the cluster pericenter time (Figure 9).

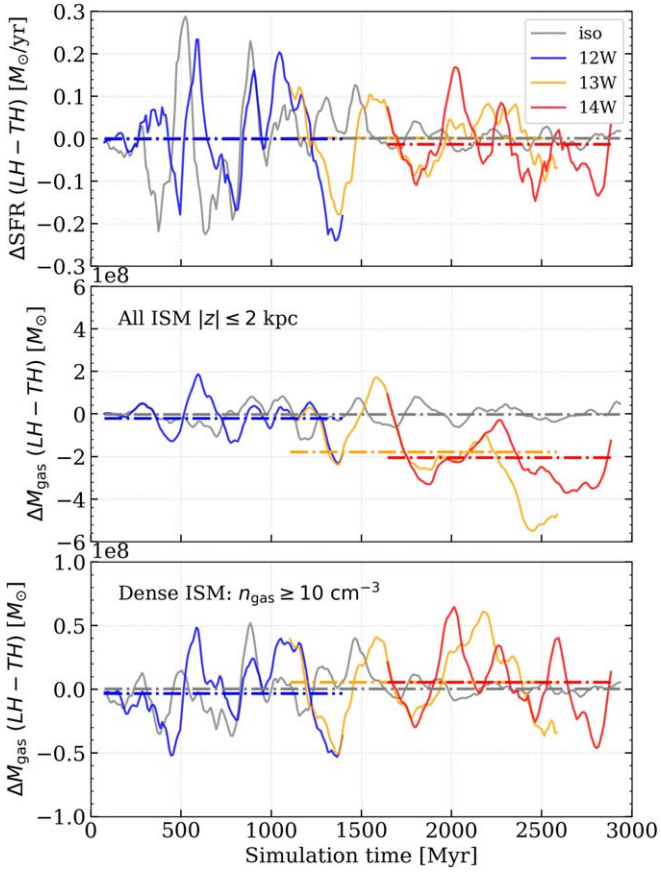

Figure 14. The SFR and gas mass differences between the LH and TH vs. simulation time. The three panels from top to bottom show the differences (LH minus TH) in SFR, the disk ISM mass, and the dense ISM mass (where number density exceeds the star formation threshold; see Section 2), respectively. In each panel, the solid curves show the running means over 100 Myr, and the horizontal dashed–dotted lines show the time averages of individual simulations.

ram pressure; see the time averages of iso (horizontal-gray-dashed–dotted line). Under ram pressure, the time-averaged SFR remains close to equal between the two halves (top panel); the disk ISM mass shows a strong excess in the TH under intermediate and strong ram pressure (middle panel); but the dense, star-forming ISM (bottom panel) mass is again almost equal between the two halves. The temporal trends of the SFR generally follow those of the dense ISM; they are much less sensitive to the total ISM, which acquired the strongest LH-TH disparity from RPS.

The primary effect of RPS (with an edge-on component) is generating an excess of low-density gas in the TH that has a low contribution to the global SFR (Figure 13). The SFR and dense ISM of the two halves, although subject to temporal oscillations, show close to equal time-averaged values and no trend with respect to ram pressure (Figure 14). Our finding of the RPS-driven gas excess in the TH agrees with Troncoso-Iribarren et al. (2020), but our interpretation of this asymmetry differs. Since Troncoso-Iribarren et al. (2020) defined the star formation efficiency of each half as the mass-weighted SFR/M_{gas}, the TH efficiency may be biased by the excess of non-star-forming gas, appearing as an efficiency enhancement in the LH. We showed that the dense ISM responsible for star formation shows no such disparity (Figure 14), indicating that the likely more compressed LH has the same efficiency as the TH.

To conclude, compression is not the direct cause of the ram pressure-induced SFR enhancement in our simulations, judging from two independent tests, (i) the spatially resolved SFR surface densities (Σ_{SFR}) in the stripping set show no systematic enhancement at comparable Σ_{gas} (inferred from the KS relation; Figures 10 and 11), (ii) galaxy-scale global properties, SFR and dense ISM mass, show no enhancement in the LH where compression is stronger. Instead, the RPS-induced mass flows (Figures 7 and 8) account for the centralized mass and SFR profiles (Figures 9 and 13), which supports mass transport as the direct mechanism for the SFR enhancement.

5.2. Predictions for Observations

Here we predict RPS observables based on the simulation results, where Section 5.2.1 focuses on the surviving gas in the disk and Section 5.2.2 on the local SFR–mass relations. We will discuss our predictions in the context of recent environmental surveys, GASP (Poggianti et al. 2017; Moretti et al. 2020; Vulcani et al. 2020) and VERTICO (Brown et al. 2021; Jiménez-Donaire et al. 2023).

5.2.1. Surviving Gas in the Disk: The Dense Gas Ratio and the Gas Mass Fraction

We describe the surviving gas using two global quantities: the dense gas ratio ($R_{\Sigma_{10}}$) and the gas mass fraction (f_{gas}) within

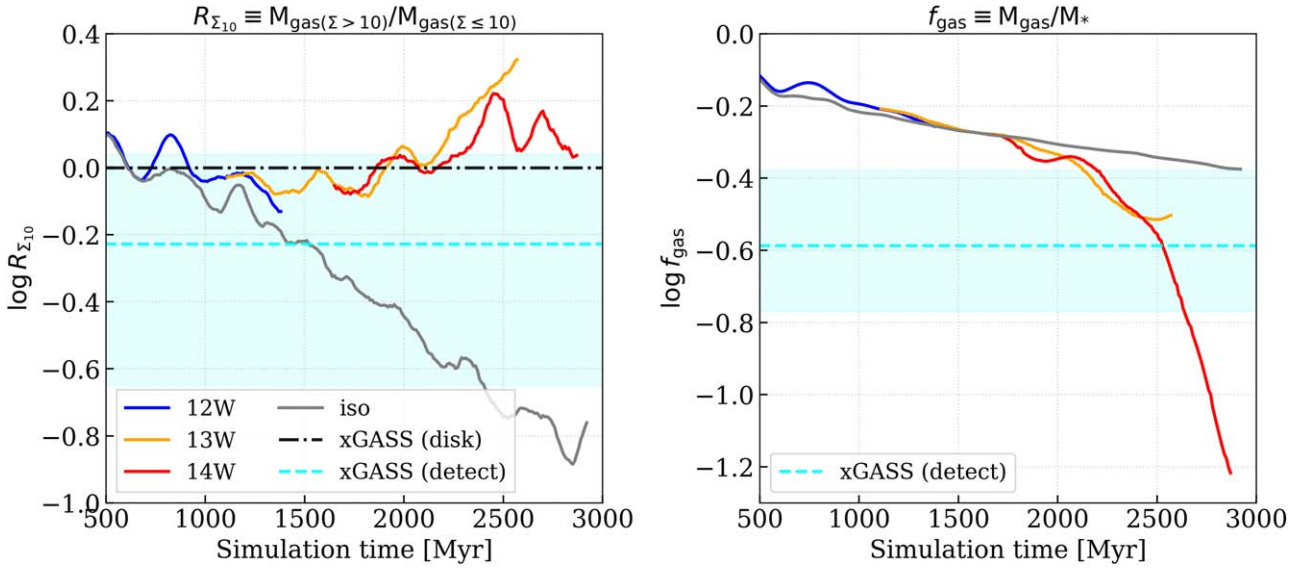

Figure 15. Time evolution of the dense gas ratio $R_{\Sigma_{10}}$ (left) and the gas mass fraction f_{gas} (right). For the dense gas ratio, we employed a simplified $\Sigma_{gas} = 10\,M_\odot\,pc^{-2}$ cut to distinguish the H I- and H_2-dominated gas; see Section 5.2. The dashed–dotted line in the left panel shows the average $M_{H_2}/M_{H\,I}$ ratio for the disk regions of the xGASS sample (see Figure 3 of Moretti et al. 2020). The cyan-dashed lines and shadings on both panels show the median and the first to third quartile ranges of the xGASS sample (Saintonge et al. 2017; Catinella et al. 2018) at a comparable stellar mass range ($9.6 < \log M_*/M_\odot < 9.9$). All simulation quantities are for the disk only (disk height $|z| \leqslant 2$ kpc; excluding the stripping tails).

the simulated disk. The dense gas ratio is an estimate for the H_2 to H I mass ratio, defined as $R_{\Sigma_{10}} \equiv M_{gas(\Sigma_{gas}>10)}/M_{gas(\Sigma_{gas}\leqslant 10)}$, where $\Sigma_{gas} = 10\,M_\odot\,pc^{-2}$ is adopted as an empirical atomic-to-molecular transition density (Krumholz et al. 2009; Kennicutt & Evans 2012; also see Section 4.2). The ratio $R_{\Sigma_{10}}$ is not a direct modeling of $M_{H_2}/M_{H\,I}$, but it self-consistently compares the molecular- and atomic-dominated gas masses in our simulations. The gas mass fraction is defined as $f_{gas} \equiv M_{gas}/M_*$, where M_{gas} is the total gas mass within the disk and M_* includes the static stellar potential (Section 2) and the formed star particles. Figure 15 shows the time evolution of both quantities, for which we consistently selected disk height $|z| \leqslant 2$ kpc, hence excluding most of the unbound gas in the tail.

In Figure 15, we annotated the observational results from the extended GALEX Arecibo SDSS Survey (xGASS; Catinella et al. 2018) as a reference. The comparison sample we adopted (cyan in both panels, dashed line for median, shading for first to three quartiles) is a subset of 21 xGASS galaxies with comparable stellar masses ($M_* \in 10^{9.6-9.9} M_\odot$) to our simulated satellite galaxy, and with detections in both CO and H I (Saintonge et al. 2017; Catinella et al. 2018). We consistently adopted $M_{H_2}/M_{H\,I}$ as the dense gas ratio (left panel) for the observational samples. Additionally, we showed the average dense gas ratio of xGASS disk regions (dashed–dotted line; following Moretti et al. 2020), which has an additional disk radius selection (Wang et al. 2020) that results in a higher dense gas ratio.

In our simulations, the dense gas ratio $R_{\Sigma_{10}}$ in the RPS cases is consistently higher than that in the isolated galaxy case (Figure 15, left panel). The ratio $R_{\Sigma_{10}}$ increases with time in 13W and 14W, as opposed to the clearly decreasing trend in iso. The decreasing trend in iso is a result of starvation (Figure 11): gas depletion due to star formation and feedback favors the high Σ_{gas} regions with high local Σ_{SFR}, reducing the ratio of the denser (e.g., $\Sigma_{gas} > 10\ M_\odot\,pc^{-2}$; H_2-dominated) gas. While in the RPS cases, gas removal favors the low Σ_{gas} regions where the gravitational restoring force is weakest (*outside-in stripping*), and the central disk regions can be replenished by the ram-pressure-driven mass flows like fallback and radial inflows (Section 5.1)—both mechanisms increasing the dense gas ratio within the disk. Compared at the pericenter times (Table 5), $R_{\Sigma_{10}}$ in 13W and 14W are 1.04 and 0.87 dex higher than iso (a factor of 11.0 and 7.5), respectively.

Our result that RPS can increase the dense gas ratio agrees with Moretti et al. (2020), who found a factor of 4 to ∼100 higher $M_{H_2}/M_{H\,I}$ ratios for three GASP jellyfish galaxies (undergoing active RPS) than the xGASS disk control sample (dashed–dotted line in Figure 15). Moretti et al. (2020) suggested that a more efficient conversion of neutral into molecular gas in these jellyfish galaxies can explain their significantly higher molecular mass ratios. However, the $R_{\Sigma_{10}}$ trends in our simulations can be explained by the different gas depletion models under starvation versus RPS described above, independent of the H I–H_2 conversion. Despite the different definitions, our $R_{\Sigma_{10}}$ values are comparable with the observational $M_{H_2}/M_{H\,I}$ values of the xGASS sample (Figure 15); we do not see the high $M_{H_2}/M_{H\,I} \gtrsim 10$ ($\log R_{\Sigma_{10}} > 1$) of the three jellyfish galaxies in Moretti et al. (2020).

The evolution of the gas mass fraction f_{gas} (Figure 15, right panel) closely follows that of M_{gas} (Figure 3) because the stellar mass evolution is relatively minimal throughout the simulations ($M_* = 10^{9.7-9.8}\,M_\odot$). The initial condition of $\log f_{gas} \approx 0$ we adopted (Section 2.1) is ∼0.5 dex higher than the xGASS average value ($0.01 < z < 0.05$ galaxies (Catinella et al. 2018) but within 1σ of that in Calette et al. 2018), otherwise the f_{gas} evolution throughout the iso simulation is within the observational scatter of xGASS (cyan shading in Figure 15). We take $f_{gas}(t)$ in iso as the reference gas fraction in our simulations: 12W is in overall agreement with iso, 13W at the group pericenter is mildly lower ($\Delta \log f_{gas} \approx -0.16$ dex), and 14W at the cluster pericenter is significantly lower (−0.84 dex). As expected, direct removal by RPS decreases the total M_{gas} and

hence $f_{\rm gas}$ in the group and cluster cases. But in the group case, a -0.16 dex deviation from prediction is within the typical observational scatter (0.2–0.3 dex) of such relations (see Figure 15 and Cortese et al. 2021, Figure 2). The satellite at 13W pericenter has a reduced gas fraction but still belongs to the gas normal regime, while at 14W, it is gas deficient during the final ∼400 Myr approaching the pericenter.

For the simulation cases with observable gas stripping morphology (13W and 14W), RPS always reduces $f_{\rm gas}$ in the galaxy disks. This means that under RPS, despite the mass transfer channels that can potentially replenish the dense/central disk gas, stripping of the low-density/outer disk gas dominates the global mass evolution (see, e.g., Figure 7). But when we account for the total gas in the disk *and tail* (tail gas potentially unbound), we find, similarly to Moretti et al. (2020), that $f_{\rm gas,disk+tail}$ is similar between the RPS and iso cases.

To summarize Section 5.2.1, first, RPS with an edge-on component tends to increase the dense gas ratio in the disk, while starvation decreases it. This could explain the observed higher molecular-to-atomic gas ratio ($M_{\rm H_2}/M_{\rm H\,I}$) in jellyfish galaxies (Moretti et al. 2020) without requiring a substantially higher H I–H_2 conversion efficiency. Second, RPS (unsurprisingly) reduces the gas mass fractions in the disk, even where the global SFR is enhanced. Where ram pressure at the orbital pericenter is insufficient to remove the densest ISM (13W), the $f_{\rm gas}$ reduction can be mild, maintaining the stripped galaxy in the gas normal regime ($< \pm 0.3$ dex). The remaining gas in the disk at 13W pericenter will likely be perturbed by galaxy-galaxy gravitational interactions, which are expected to be effective in group environments; see Section 5.3.

5.2.2. RPS Signatures on the Local SFR–Mass Relations

High angular resolution observations have enabled the direct mapping of galactic star formation laws on small scales (Bigiel et al. 2008; Leroy et al. 2008; Kennicutt & Evans 2012). Some recent programs include the Physics at High Angular resolution in Nearby GalaxieS survey for nearby galaxies (Leroy et al. 2021; Lee et al. 2022), the VERTICO survey for Virgo cluster galaxies (Brown et al. 2021; Jiménez-Donaire et al. 2023), and the GASP survey for environmentally selected jellyfish galaxies (Poggianti et al. 2017; Jaffé et al. 2018; Moretti et al. 2020; Vulcani et al. 2020). RPS is one of the main environmental processes in the environmentally selected samples (e.g., GASP and VERTICO), but the assessment of the RPS impact often faces several challenges: (i) the inevitable mixture of sample stellar masses and inclination angles, (ii) the difficulties of constraining the environment (e.g., ICM densities) and the satellite orbits, and (iii) the complex gravitational effects that could coexist with RPS. Here, we use our simulation suite, which focuses on a single galaxy across various environments undergoing RPS and no tidal effects, to make predictions for the observational *RPS signatures* on the local SFR–mass relations.

To create mock observational data sets, we selected 900 Myr of simulation data (90 outputs) that cover more than 3 dex of $P_{\rm ram}$ in the wind runs (Figure 2), ranging over 1.5 Gyr in simulation time. Stacking the selected data creates two data sets, the stripping set and the isolated control set. This is equivalent to observing an ensemble of galaxies at $M_* \approx 10^{9.7-9.8}\,M_\odot$ undergoing various stages of RPS (stripping set: Milky Way–like to cluster pericenter environments) or starvation (isolated control set: ∼1.5 Gyr duration). Figure 16 shows the local SFR–mass relations for the two sets on a 1 $\rm kpc^2$ scale, following the methodology described in Section 4. In Figure 16, we shaded the low SFR regions where $\log \Sigma_{\rm SFR}$ are below observational limits (~ -4 dex, e.g., Kennicutt & Evans 2012; Leroy et al. 2012; Vulcani et al. 2020). The over-densities in the simulation data at certain low $\Sigma_{\rm SFR}$ is a numerical effect due to our star particle mass resolution (e.g., the lowest horizontal over-density corresponds to the $\Sigma_{\rm SFR}$ from a single star particle of $\approx 800\,M_\odot$). To guide observational comparison, we show the global KS relation for the 61 non-starburst spiral galaxies from Kennicutt (1998) in the left panel in addition to the resolved KS relations from Bigiel et al. (2008); also see Figure 10. The discontinuous sampling at high Σ_* (right panel) is caused by the limited 1 $\rm kpc^2$ spatial patch number in the disk center.

The resolved KS relation for the time-stacked stripping and iso sets is remarkably consistent (Figure 16, left panel). When observed at different snapshots in time (e.g., in Figures 10 and 11), the galaxy populates different $\Sigma_{\rm gas}$ ranges, which are closely correlated with the local $\Sigma_{\rm SFR}$ (Section 4.2). In the time-stacked view, where the $\Sigma_{\rm gas}$ ranges become similar between the two sets, the underlying KS relation is in overall agreement. Our finding is consistent with Jiménez-Donaire et al. (2023; VERTICO) results that the local KS relation agrees between an ensemble of Virgo RPS satellites and their isolated field counterparts, which suggests that RPS does not directly affect the local star formation efficiency within the gas.

The main difference between the stripping and isolated control sets is best seen in the 1D distributions of $\Sigma_{\rm gas}$ and $\Sigma_{\rm SFR}$. The stripping set reaches higher maximum surface densities and is truncated at low surface densities; the peaks in both $\Sigma_{\rm gas}$ and $\Sigma_{\rm SFR}$ distribution are at higher values compared with the isolated set. The difference can be explained by a combination of low-density gas removal and high-density gas replenishment in the stripping set; see the evolution of the dense gas ratio (Section 5.2.1). Another relatively minor difference is that the stripping set reaches higher $\Sigma_{\rm SFR}$ at low $\Sigma_{\rm gas}$ (<0 dex), which, as also discussed above, is likely due to fast gas removal by RPS in still star-forming regions. The signals of high $\Sigma_{\rm SFR}$ at low $\Sigma_{\rm gas}$ only occur shortly before the complete removal of gas (cluster pericenter in Figure 10).

The time-stacked star formation main sequence relation (Figure 16 right panel) shows a mild $\Sigma_{\rm SFR}$ enhancement over a range of Σ_* in the stripping set. Independent of RPS or starvation, the Σ_* radial profiles remain monotonic (Figure 9), so the local Σ_* can be used as an indicator of disk radii. Under increasing ram pressure, the Σ_* threshold where the wind SFR exceeds iso SFR increases (corresponding disk radius decreases), so the time-stacked result here shows a smoother $\Sigma_{\rm SFR}$ enhancement that extends to lower Σ_* (larger radii) compared with the group and cluster pericenter cases (Figure 12). This agrees with the Vulcani et al. (2020; GASP) finding that $\Sigma_{\rm SFR}$ can be enhanced over a range of Σ_* when accounting for various stripping stages. However, at the lowest Σ_* end, where Vulcani et al. (2020) found SFR enhancement in the stripping sample, our simulations always show disk truncation (lowest Σ_* not populated in the stripping set; Section 4.3), instead of SFR enhancement. We note that since we focused on the disk region ($|z| \leqslant 2$ kpc), our sampled patches are free of star-forming clumps in the tail, which are shown to have a higher $\Sigma_{\rm SFR}$ than the disk at low Σ_* (Vulcani et al. 2020).

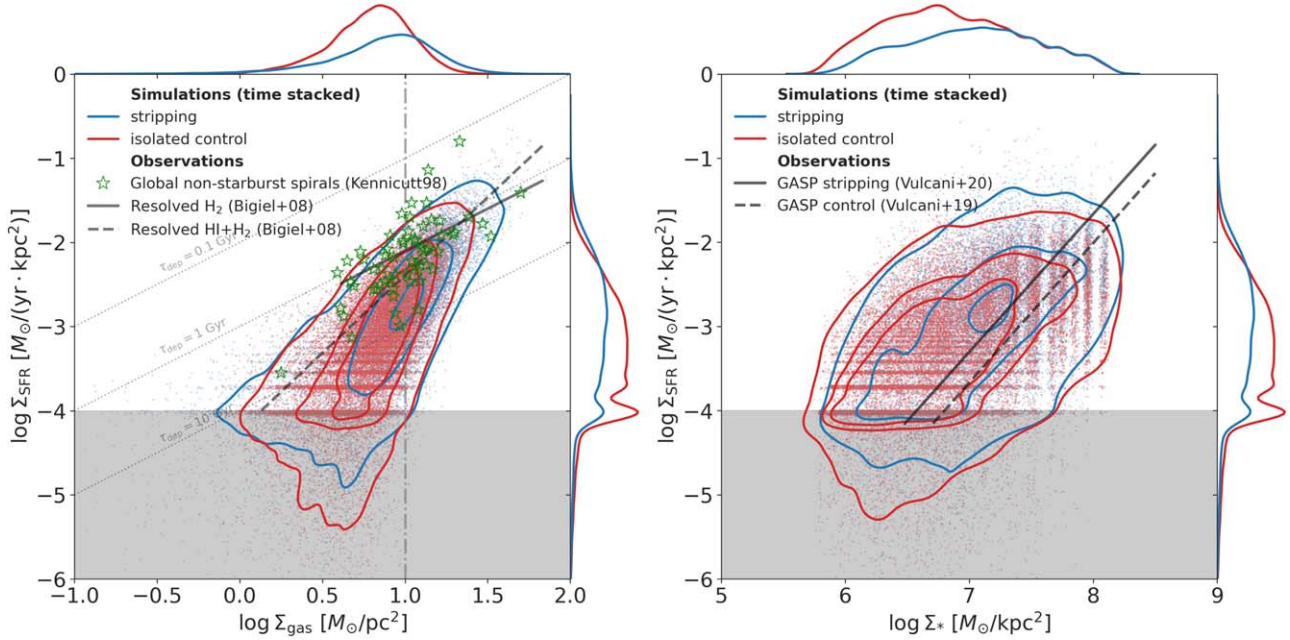

Figure 16. Spatially resolved SFR–mass relations (KS and star formation main sequence; see Section 4), similar to Figures 10 and 12. Here for the observational predictions, we stacked 900 Myr of simulation data (90 outputs), covering more than 3 dex of ram pressure strengths in the wind runs (Section 5.2). The shaded regions in both panels are where $\log \Sigma_{\rm SFR}$ is below current observational limits (~ -4 dex). In the left panel, we additionally show the global KS relation of the non-starburst spiral galaxies from Kennicutt (1998), see Section 5.2.2.

Our predictions in Section 5.2.2 can be summarized as follows. When observing a large ensemble of RPS and isolated galaxies at the same stellar mass, the set of galaxies undergoing RPS will have the same KS relation with the isolated control set at comparable gas surface densities. Individual galaxies may populate different $\Sigma_{\rm gas}$ ranges and hence occupy different subsets of the ensemble KS relation, which can be caused by both active (RPS-driven gas flows) and passive (gas consumption due to starvation) mechanisms, as shown in Figure 11. However, there is no evidence of star formation efficiency change at given $\Sigma_{\rm gas}$ in the RPS cases. On the star formation main sequence plane ($\Sigma_{\rm SFR}$–Σ_*), the RPS galaxy disks (clear of tail contamination and inclination/projection effects) will show enhanced $\Sigma_{\rm SFR}$ above a certain Σ_* threshold, and sparse sampling indicating disk truncation below the Σ_* threshold. This is because galaxies undergoing RPS tend to have more centrally concentrated gas (and SFR) radial profiles than their isolated counterparts under starvation (e.g., Figure 9). All predictions here assume that RPS is the only active effect and starvation is the only passive effect. We discuss how these assumptions are limited and their implications in Section 5.3 below.

5.3. Limitations

We made idealistic simplifications in our modeling choices in order to focus on the science goals. We adopted a single star formation and feedback recipe (Goldbaum et al. 2015, 2016) and a static dark matter potential, omitted the direct modeling of magnetic fields, turbulence, and cosmic rays, and only sampled a single (most probable; Wetzel 2011) satellite orbit and a 45° wind inclination in each halo, instead of conducting a population study. In particular, we discuss the following two and their implications.

(i) Gas removal by gravitational mechanisms. Our controlled suite of hydrodynamical simulations only includes active gas removal by RPS; we are missing the gravitational mechanisms, including satellite–host and satellite–satellite interactions (Boselli & Gavazzi 2006). In clusters, RPS by the ICM is the dominant mechanism for cold gas stripping (Boselli & Gavazzi 2006; Cortese et al. 2021). In galaxy groups (lower relative velocities), satellite–satellite gravitational interactions are traditionally considered the primary stripping mechanism based on the observational evidence in various systems (e.g., Yun et al. 1994; Serra et al. 2013; Lee-Waddell et al. 2019; Wang et al. 2022). However, the observational selection bias toward gas-rich galaxies in groups may have favored the gravitational mechanisms (Cortese et al. 2021); in fact, both simulations (Bekki 2014; Bahé & McCarthy 2015; Marasco et al. 2016) and recent observational work (Putman et al. 2021; Roberts et al. 2021; Kolcu et al. 2022) have found that RPS can be efficient in galaxy groups. RPS and gravitational (satellite–satellite) interactions are likely both effective in groups, and the relative importance depends on individual environments and satellites.

Missing the aspect of gravitational interactions, we likely overestimated the final $M_{\rm gas}$ (and $f_{\rm gas}$) in our galaxy group case (13W; Figures 3 and 15), as gravitational encounters can contribute to active gas removal. As the satellite still retains some ISM at the 13W pericenter, gravitational interactions will additionally perturb the remaining gas, affecting its morphology and kinematics (Figures 5 and 6), and cause disturbances in the stellar disk. Such effects may also be present in the Milky Way and cluster halo cases but will have a weaker impact on the global properties (low likelihood of massive galaxy-galaxy close encounters in a Milky Way–like halo; high relative velocities in clusters).

Gravitational interactions will not change our key result of the RPS-induced star formation enhancement. Gas stripping by gravitational mechanisms is *outside in* (like RPS), and will have a relatively minimal impact on the dense gas in the disk center, where the SFR enhancement occurs in our simulations

(e.g., Figures 9 and 12). Our result is overall consistent with current observational evidence of triggered star formation that is of RPS origin, including global and local SFR enhancement (Vulcani et al. 2018, 2020; Roberts & Parker 2020), and star formation in the tail (Hester et al. 2010; Ebeling et al. 2014; Poggianti et al. 2019).

(ii) Passive gas depletion and accretion. We modeled passive gas depletion (i.e., free of direct removal) in our isolated galaxy simulation: steady consumption by star formation and stellar and supernova feedback-driven outflows. This scenario, however, only applies to a special case of galaxies where gas accretion has been halted, which we refer to as starvation following literature conventions (Larson et al. 1980). Accretion flows can naturally be halted by RPS, but they also likely occur in many of the star-forming field galaxies today, whose SFR relies on the rejuvenating cold gas accretion, e.g., via cooling inflows from the circumgalactic medium (Tumlinson et al. 2017).

Gas accretion is a fundamental aspect of galaxy evolution that remains poorly constrained (Fox & Davé 2017). With the typical inflow rates and redshift dependence being highly uncertain, direct modeling of accretion is challenging. But we can infer the impact of accretion by comparing the SFR time evolution in our simulated iso case (starvation without accretion), with the observational SFR–redshift relation (Speagle et al. 2014) at our modeled stellar mass. The difference in the SFR time evolution will characterize the star formation fueled by accretion missing in our iso simulation.

Taking the initial and final conditions in iso (Figure 3; $t_{\rm init} = 500$ Myr and $t_{\rm final} = 2980$ Myr), which converts to $t_{\rm lookback} \approx 2.5$ Gyr and the present day, the best-fit relation from Speagle et al. 2014 gives $\log{\rm SFR}_{\rm best\text{-}fit}$ of 0.07 and -0.24 dex. While in the iso simulation (starvation without accretion), the initial and final $\log{\rm SFR}_{\rm iso}$ are 0.18 and -0.46 dex, respectively. The simulation values are still within the expected scatter of $\log{\rm SFR}_{\rm best\text{-}fit}$ (± 0.3 dex; Speagle et al. 2014), but unsurprisingly decrease faster with time due to the lack of replenishment. If we use the observational best-fit value as our field galaxy control case instead, which represents the average of observed star-forming galaxies at this stellar mass, the galaxy group case (13W) still shows globally enhanced SFR, although the enhancement becomes mild (a factor of 1.5 instead of $\sim$2.5).

6. Summary and Conclusions

In this paper, we present a suite of galaxy-scale *wind tunnel* simulations with radiative cooling, star formation, and supernovae feedback, modeling a low-mass satellite galaxy undergoing RPS in various halo environments. The input time-varying ram pressure covers over three orders of magnitude (Figure 2), representing realistic satellite infall orbits from a Milky Way–like halo's R_{200} to a cluster's pericenter. We simulate the same satellite galaxy in isolation for $\sim$3 Gyr as a control case, and compare the simulations in terms of their global evolution, gas morphology and kinematics, and the spatially resolved SFR–mass relations. Our key findings can be summarized as follows.

1. RPS has the potential to quench or enhance (up to a factor of $\sim$2.5) the global SFR of a satellite galaxy while gas is being removed (Figure 3). The impact on SFR depends on both the strength and the time derivative of the ram pressure.
2. Star formation is radially centralized under a moderate (13W; group halo) or strong (14W; cluster halo) ram pressure profile, and it occurs in the stripped tail when the satellite reaches the cluster pericenter (Figure 4). This is also reflected in a central enhancement of gas density (Figure 9).
3. Under an inclined wind (with face-on *and* edge-on components), stripping in the disk outskirts dominates the gas mass loss, but when the pericentric ram pressure is insufficient for complete gas removal (13W), some stripped gas falls back and replenishes the central disk (Figures 6 and 7). The edge-on component of ram pressure also drives a direct radial gas inflow (13W and 14W; Figure 8) where it counters the disk rotation (right panel of Figure 6).

This radial gas transport has the following consequences:

4. The stripping set (13W and 14W) shows an excess of high $\Sigma_{\rm SFR}$–high $\Sigma_{\rm gas}$ material relative to the iso control set on the spatially resolved KS plane (Figure 10). However, the underlying KS relation is the same between the two sets when compared at similar $\Sigma_{\rm gas}$ (Figure 11), indicating that RPS has no direct effect on the star formation efficiency.
5. On the spatially resolved SFR–stellar mass plane, the stripping set shows enhanced $\Sigma_{\rm SFR}$ at high Σ_* (corresponding to central disk regions) relative to iso, and is truncated at the lowest Σ_* (Figure 12).
6. The dense gas ratio ($R_{\Sigma_{10}}$; an approximation for $M_{\rm H_2}/M_{\rm H\,I}$) increases with time in the stripping set because of a combination of low-density gas removal and dense gas replenishment, as opposed to the decreasing trend in iso, due to starvation (Figure 15).

Several of our findings agree with observational results. First, the RPS-induced global SFR enhancement is mild, up to a factor of $\sim$2.5 relative to iso, or $\sim$1.5 relative to the observational SFR–redshift relation (Speagle et al. 2014; see Section 5.3). This agrees with the typical enhancement factor of <2 in observational samples of RPS-triggered star formation (Iglesias-Páramo et al. 2004; Vulcani et al. 2018; Roberts & Parker 2020). Second, despite occupying different $\Sigma_{\rm gas}$ ranges, the stripping and isolated sets follow the same local KS relation, consistent with Jiménez-Donaire et al. (2023; the VERTICO survey); the stripping set's $\Sigma_{\rm SFR}$ is smoothly enhanced at high Σ_*—the inner disk, consistent with Vulcani et al. (2020; the GASP survey). Third, the stripping set acquires an enhanced dense gas ratio, which agrees with the high $M_{\rm H_2}/M_{\rm H\,I}$ ratios found for three GASP jellyfish galaxies (Moretti et al. 2020). Finally, RPS by a galaxy group medium can be effective for low-mass spiral galaxies and potentially lead to enhanced global SFR (Roberts et al. 2021; Kolcu et al. 2022).

The radial redistribution of gas in the galaxy is a key result of this work: gas is stripped from the outskirts and enhanced in the center. It is the direct cause of the SFR enhancement when $P_{\rm ram}$ is insufficient to remove the entire gas disk; when $P_{\rm ram}$ is sufficient for central gas removal, the galaxy is ultimately quenched of star formation. This mass transport scenario is consistent with the increased dense gas ratio in jellyfish galaxies (Moretti et al. 2020), the local KS relation agreement

between environmentally selected samples (Jiménez-Donaire et al. 2023), and the comparable star formation efficiency between the leading and trailing halves of the disk (Figure 14). We find that this explanation is a better match to the simulations than compression by ram pressure (Section 5.1) or a more efficient H I–H_2 conversion (Section 5.2.1)—as the main driver for potential SFR enhancement.

Acknowledgments

We thank Dan Foreman-Mackey, Mary Putman, David Schiminovich, Jacqueline van Gorkom, and Ann Zabludoff for helpful discussions. We thank the anonymous referee for useful suggestions that improved the paper. J.Z. thanks Matthew Abruzzo, Nina Akerman, and Hui Li for the conversations on the simulations. S.T. thanks the GASP Collaboration for useful conversations. G.L.B. acknowledges support from the NSF (AST-2108470, XSEDE), a NASA TCAN award, and the Simons Foundation through the Learning the Universe Simons Collaboration. The simulations used in this work were run and analyzed on facilities supported by the Scientific Computing Core at the Flatiron Institute, a division of the Simons Foundation. We also acknowledge computing resources from Columbia University's Shared Research Computing Facility project, which is supported by NIH Research Facility Improvement Grant 1G20RR030893-01, and associated funds from the New York State Empire State Development, Division of Science Technology and Innovation (NYSTAR) Contract C090171, both awarded on 2010 April 15. Analyses of this work have made use of NumPy (Harris et al. 2020), Astropy (Astropy Collaboration et al. 2013, 2018, 2022), yt (Turk et al. 2011), and Ipython (Perez & Granger 2007).

ORCID iDs

Jingyao Zhu https://orcid.org/0000-0002-9001-6713
Stephanie Tonnesen https://orcid.org/0000-0002-8710-9206
Greg L. Bryan https://orcid.org/0000-0003-2630-9228

References

Abadi, M. G., Moore, B., & Bower, R. G. 1999, MNRAS, 308, 947
Akerman, N., Tonnesen, S., Poggianti, B. M., Smith, R., & Marasco, A. 2023, ApJ, 948, 18
Anderson, M. E., & Bregman, J. N. 2011, ApJ, 737, 22
Appleby, S., Davé, R., Kraljic, K., Anglés-Alcázar, D., & Narayanan, D. 2020, MNRAS, 494, 6053
Arnaud, M. 2009, A&A, 500, 103
Astropy Collaboration, Price-Whelan, A. M., Lim, P. L., et al. 2022, ApJ, 935, 167
Astropy Collaboration, Price-Whelan, A. M., Sipőcz, B. M., et al. 2018, AJ, 156, 123
Astropy Collaboration, Robitaille, T. P., Tollerud, E. J., et al. 2013, A&A, 558, A33
Bahé, Y. M., & McCarthy, I. G. 2015, MNRAS, 447, 969
Bahé, Y. M., McCarthy, I. G., Crain, R. A., & Theuns, T. 2012, MNRAS, 424, 1179
Bahé, Y. M., Schaye, J., Barnes, D. J., et al. 2019, MNRAS, 485, 2287
Baldry, I. K., Balogh, M. L., Bower, R. G., et al. 2006, MNRAS, 373, 469
Bekki, K. 2014, MNRAS, 438, 444
Bigiel, F., Leroy, A., Walter, F., et al. 2008, AJ, 136, 2846
de Blok, W. J. G., Walter, F., Brinks, E., et al. 2008, AJ, 136, 2648
Boselli, A., Boissier, S., Cortese, L., et al. 2006, ApJ, 651, 811
Boselli, A., & Gavazzi, G. 2006, PASP, 118, 517
Brown, T., Wilson, C. D., Zabel, N., et al. 2021, ApJS, 257, 21
Bryan, G. L., Norman, M. L., O'Shea, B. W., et al. 2014, ApJS, 211, 19
Burkert, A. 1995, ApJL, 447, L25
Calette, A. R., Avila-Reese, V., Rodríguez-Puebla, A., Hernández-Toledo, H., & Papastergis, E. 2018, RMxAA, 54, 443
Catinella, B., Saintonge, A., Janowiecki, S., et al. 2018, MNRAS, 476, 875
Cavaliere, A., & Fusco-Femiano, R. 1976, A&A, 49, 137
Choi, W., Kim, C.-G., & Chung, A. 2022, ApJ, 936, 133
Cortese, L., Catinella, B., & Smith, R. 2021, PASA, 38, e035
Croton, D. J., Springel, V., White, S. D. M., et al. 2006, MNRAS, 365, 11
Crowl, H. H., & Kenney, J. D. P. 2008, AJ, 136, 1623
Dai, X., Anderson, M. E., Bregman, J. N., & Miller, J. M. 2012, ApJ, 755, 107
Dalla Vecchia, C., & Schaye, J. 2008, MNRAS, 387, 1431
Deb, T., Verheijen, M. A. W., Poggianti, B. M., et al. 2022, MNRAS, 516, 2683
Donnari, M., Pillepich, A., Joshi, G. D., et al. 2021a, MNRAS, 500, 4004
Donnari, M., Pillepich, A., Nelson, D., et al. 2021b, MNRAS, 506, 4760
Ebeling, H., Stephenson, L. N., & Edge, A. C. 2014, ApJL, 781, L40
Fox, A., & Davé, R. 2017, Gas Accretion onto Galaxies, Vol. 430 (Berlin: Springer)
Goldbaum, N. J., Krumholz, M. R., & Forbes, J. C. 2015, ApJ, 814, 131
Goldbaum, N. J., Krumholz, M. R., & Forbes, J. C. 2016, ApJ, 827, 28
Gunn, J. E., & Gott, J. R., III 1972, ApJ, 176, 1
Haardt, F., & Madau, P. 2012, ApJ, 746, 125
Haines, C. P., Pereira, M. J., Smith, G. P., et al. 2015, ApJ, 806, 101
Harris, C. R., Millman, K. J., van der Walt, S. J., et al. 2020, Natur, 585, 357
Heiderman, A., Evans, N. J., II, Allen, L. E., Huard, T., & Heyer, M. 2010, ApJ, 723, 1019
Hester, J. A., Seibert, M., Neill, J. D., et al. 2010, ApJL, 716, L14
Iglesias-Páramo, J., Boselli, A., Gavazzi, G., & Zaccardo, A. 2004, A&A, 421, 887
Jáchym, P., Kenney, J. D. P., Sun, M., et al. 2019, ApJ, 883, 145
Jáchym, P., Palouš, J., Köppen, J., & Combes, F. 2007, A&A, 472, 5
Jaffé, Y. L., Poggianti, B. M., Moretti, A., et al. 2018, MNRAS, 476, 4753
Jiménez-Donaire, M. J., Brown, T., Wilson, C. D., et al. 2023, A&A, 671, A3
Jung, S. L., Choi, H., Wong, O. I., et al. 2018, ApJ, 865, 156
Kapferer, W., Sluka, C., Schindler, S., Ferrari, C., & Ziegler, B. 2009, A&A, 499, 87
Kauffmann, G., White, S. D. M., Heckman, T. M., et al. 2004, MNRAS, 353, 713
Kennicutt, R. C., & Evans, N. J. 2012, ARA&A, 50, 531
Kennicutt, R. C., Jr. 1989, ApJ, 344, 685
Kennicutt, R. C., Jr. 1998, ApJ, 498, 541
Kolcu, T., Crossett, J. P., Bellhouse, C., & McGee, S. 2022, MNRAS, 515, 5877
Komatsu, E., & Seljak, U. 2001, MNRAS, 327, 1353
Kruijssen, J. M. D., & Longmore, S. N. 2014, MNRAS, 439, 3239
Kruijssen, J. M. D., Schruba, A., Hygate, A. P. S., et al. 2018, MNRAS, 479, 1866
Krumholz, M. R., Dekel, A., & McKee, C. F. 2012, ApJ, 745, 69
Krumholz, M. R., McKee, C. F., & Tumlinson, J. 2009, ApJ, 693, 216
Larson, R. B., Tinsley, B. M., & Caldwell, C. N. 1980, ApJ, 237, 692
Lee, J., Kimm, T., Katz, H., et al. 2020, ApJ, 905, 31
Lee, J. C., Whitmore, B. C., Thilker, D. A., et al. 2022, ApJS, 258, 10
Lee-Waddell, K., Koribalski, B. S., Westmeier, T., et al. 2019, MNRAS, 487, 5248
Lelli, F., McGaugh, S. S., Schombert, J. M., Desmond, H., & Katz, H. 2019, MNRAS, 484, 3267
Leroy, A. K., Bigiel, F., de Blok, W. J. G., et al. 2012, AJ, 144, 3
Leroy, A. K., Schinnerer, E., Hughes, A., et al. 2021, ApJS, 257, 43
Leroy, A. K., Walter, F., Brinks, E., et al. 2008, AJ, 136, 2782
Lovisari, L., Reiprich, T. H., & Schellenberger, G. 2015, A&A, 573, A118
Ludlow, A. D., Navarro, J. F., Angulo, R. E., et al. 2014, MNRAS, 441, 378
Makino, N., Sasaki, S., & Suto, Y. 1998, ApJ, 497, 555
Marasco, A., Crain, R. A., Schaye, J., et al. 2016, MNRAS, 461, 2630
McCarthy, I. G., Frenk, C. S., Font, A. S., et al. 2008, MNRAS, 383, 593
McGaugh, S. S., Lelli, F., Schombert, J. M., et al. 2021, AJ, 162, 202
Miller, M. J., & Bregman, J. N. 2013, ApJ, 770, 118
Miller, M. J., & Bregman, J. N. 2015, ApJ, 800, 14
Miyamoto, M., & Nagai, R. 1975, PASJ, 27, 533
Molnár, D. C., Serra, P., van der Hulst, T., et al. 2022, A&A, 659, A94
Moretti, A., Paladino, R., Poggianti, B. M., et al. 2020, ApJL, 897, L30
Mori, M., & Burkert, A. 2000, ApJ, 538, 559
Navarro, J. F., Frenk, C. S., & White, S. D. M. 1996, ApJ, 462, 563
O'Sullivan, E., Ponman, T. J., & Collins, R. S. 2003, MNRAS, 340, 1375
Peng, Y.-j., Lilly, S. J., Kovač, K., et al. 2010, ApJ, 721, 193
Peng, Y.-j., Lilly, S. J., Renzini, A., & Carollo, M. 2012, ApJ, 757, 4
Perez, F., & Granger, B. E. 2007, CSE, 9, 21

Phillips, J. I., Wheeler, C., Boylan-Kolchin, M., et al. 2014, MNRAS, 437, 1930
Pillepich, A., Springel, V., Nelson, D., et al. 2018, MNRAS, 473, 4077
Poggianti, B. M., Fasano, G., Omizzolo, A., et al. 2016, AJ, 151, 78
Poggianti, B. M., Gullieuszik, M., Tonnesen, S., et al. 2019, MNRAS, 482, 4466
Poggianti, B. M., Moretti, A., Gullieuszik, M., et al. 2017, ApJ, 844, 48
Price-Whelan, A., Sipőcz, B., Lenz, D., et al. 2020, adrn/gala: v1.3, Zenodo, doi:10.5281/zenodo.4159870
Price-Whelan, A. M. 2017, JOSS, 2, 388
Putman, M. E., Zheng, Y., Price-Whelan, A. M., et al. 2021, ApJ, 913, 53
Quilis, V., Moore, B., & Bower, R. 2000, Sci, 288, 1617
Roberts, I. D., & Parker, L. C. 2020, MNRAS, 495, 554
Roberts, I. D., van Weeren, R. J., McGee, S. L., et al. 2021, A&A, 650, A111
Roberts, I. D., Lang, M., Trotsenko, D., et al. 2022, ApJ, 941, 77
Roediger, E., & Brüggen, M. 2006, MNRAS, 369, 567
Roediger, E., Bruggen, M., Owers, M. S., Ebeling, H., & Sun, M. 2014, MNRAS Lett., 443, L114
Rohr, E., Pillepich, A., Nelson, D., et al. 2023, MNRAS, 524, 3502
Ruggiero, R., & Lima Neto, G. B. 2017, MNRAS, 468, 4107
Saintonge, A., Catinella, B., Tacconi, L. J., et al. 2017, ApJS, 233, 22
Salem, M., Besla, G., Bryan, G., et al. 2015, ApJ, 815, 77
Salucci, P., & Burkert, A. 2000, ApJL, 537, L9
Sargent, M. T., Daddi, E., Béthermin, M., et al. 2014, ApJ, 793, 19
Schiminovich, D., Wyder, T. K., Martin, D. C., et al. 2007, ApJS, 173, 315
Schmidt, M. 1959, ApJ, 129, 243
Schulz, S., & Struck, C. 2001, MNRAS, 328, 185
Serra, P., Koribalski, B., Duc, P.-A., et al. 2013, MNRAS, 428, 370
Smith, B. D., Bryan, G. L., Glover, S. C. O., et al. 2017, MNRAS, 466, 2217
Speagle, J. S., Steinhardt, C. L., Capak, P. L., & Silverman, J. D. 2014, ApJS, 214, 15
Steinhauser, D., Schindler, S., & Springel, V. 2016, A&A, 591, A51
Sun, M., Donahue, M., & Voit, G. M. 2007, ApJ, 671, 190
Swaters, R. A., van Albada, T. S., van der Hulst, J. M., & Sancisi, R. 2002, A&A, 390, 829
Tasker, E. J., & Bryan, G. L. 2006, ApJ, 641, 878
Tonnesen, S., & Bryan, G. L. 2009, ApJ, 694, 789
Tonnesen, S., & Bryan, G. L. 2010, ApJ, 709, 1203
Tonnesen, S., & Bryan, G. L. 2012, MNRAS, 422, 1609
Tremmel, M., Quinn, T. R., Ricarte, A., et al. 2019, MNRAS, 483, 3336
Troncoso-Iribarren, P., Padilla, N., Santander, C., et al. 2020, MNRAS, 497, 4145
Trussler, J., Maiolino, R., Maraston, C., et al. 2020, MNRAS, 491, 5406
Tumlinson, J., Peeples, M. S., & Werk, J. K. 2017, ARA&A, 55, 389
Turk, M. J., Smith, B. D., Oishi, J. S., et al. 2011, ApJS, 192, 9
van den Bosch, F. C., Aquino, D., Yang, X., et al. 2008, MNRAS, 387, 79
van Gorkom, J. H. 2004, in Clusters of Galaxies: Probes of Cosmological Structure and Galaxy Evolution, ed. J. S. Mulchaey, A. Dressler, & A. Oemler (Cambridge: Cambridge Univ. Press), 305
Voit, G. M. 2019, ApJ, 880, 139
Vulcani, B., Poggianti, B. M., Gullieuszik, M., et al. 2018, ApJL, 866, L25
Vulcani, B., Poggianti, B. M., Moretti, A., et al. 2019, MNRAS, 488, 1597
Vulcani, B., Poggianti, B. M., Tonnesen, S., et al. 2020, ApJ, 899, 98
Wang, J., Catinella, B., Saintonge, A., et al. 2020, ApJ, 890, 63
Wang, S., Wang, J., For, B.-Q., et al. 2022, ApJ, 927, 66
Weinberger, R., Springel, V., Hernquist, L., et al. 2017, MNRAS, 465, 3291
Wetzel, A. R. 2011, MNRAS, 412, 49
Wetzel, A. R., Tinker, J. L., & Conroy, C. 2012, MNRAS, 424, 232
Wetzel, A. R., Tinker, J. L., Conroy, C., & van den Bosch, F. C. 2013, MNRAS, 432, 336
Wright, R. J., Lagos, C. d. P., Davies, L. J. M., et al. 2019, MNRAS, 487, 3740
Wu, P.-F. 2018, MNRAS, 473, 5468
Yun, K., Pillepich, A., Zinger, E., et al. 2019, MNRAS, 483, 1042
Yun, M. S., Ho, P. T. P., & Lo, K. Y. 1994, Natur, 372, 530
Zabludoff, A. I., Zaritsky, D., Lin, H., et al. 1996, ApJ, 466, 104